Selective and Synergistic Targeting of ErbB2-Positive Cancer Cells with ErbB2 Transmembrane Peptide-Ionic Liquid Nanocarrier Formulation

ACS APPLIED MATERIALS & INTERFACES

www.acsami.org

Research Article

Selective and Synergistic Targeting of ErbB2-Positive Cancer Cells with ErbB2 Transmembrane Peptide-Ionic Liquid Nanocarrier Formulation

Helal Abujubara, Pankaj Bharmoria, Dorota Raj, Samantha W. Alvarez, Siyuan Liu, Maryna Zhylinskaya, Enoch Appiah, Kasper Moth-Poulsen, Clotilde Wiel, Volkan I. Sayin, and Alesia A. Tietze*

Cite This: https://doi.org/10.1021/acsami.6c08450

Read Online

ACCESS | Metrics & More | Article Recommendations | Supporting Information

ABSTRACT: ErbB2-positive cancers are highly aggressive and remain difficult to treat due to limitations of current therapies, such as poor selectivity, insufficient delivery, and toxicity toward healthy tissues. Herein, we developed a dual-action nanoformulation combining prolinium-based surface-active ionic liquid (SAIL) nanocarriers with ErbB2-derived transmembrane (TM) peptide for selective targeting of ErbB2-positive cancer cells. Two new SAILs, which self-assemble into stable micelles/vesicles under physiological conditions, and a series of hydrophobic TM-peptides were synthesized and characterized. Among the resulting nanoformulations, **V3-BAIL** showed the strongest antiproliferative activity in ErbB2-positive breast, lung, and pancreatic cancer cell lines, whereas activity in low-ErbB2 NCI-H23 cells was minimal. The response correlated with ErbB2 expression level, demonstrating target-related selectivity. Chou-Talalay analysis revealed synergy between the SAIL nanocarrier and TM peptide. Mechanistic studies showed that **V3-BAIL** progressively accumulated in cells, reduced cellular fitness without rapid membrane lysis, and strongly suppressed PI3K/Akt and MAPK/ERK signaling. Relative to doxorubicin and cisplatin, **V3-BAIL** displayed greater selectivity toward ErbB2-positive cells, and it acted more rapidly and more strongly than trastuzumab under the tested conditions. These findings establish TM peptide-decorated SAIL nanocarriers as a promising strategy for selective and synergistic ErbB2-targeted cancer therapy.

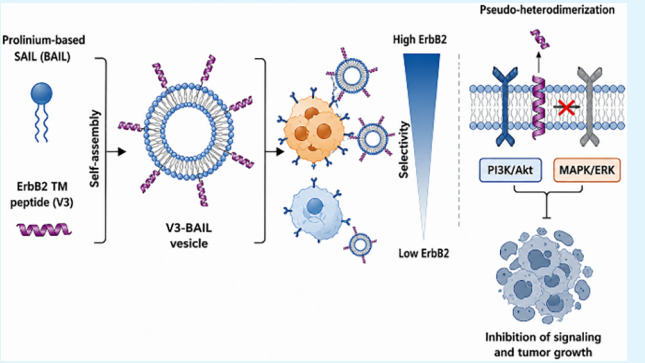

KEYWORDS: *ionic liquid, transmembrane peptide, ErbB2 cancer, epidermal growth factor receptor, nanocarrier*

INTRODUCTION

The human epidermal growth factor receptor 2 (HER2), also known as ErbB2, is overexpressed in 20% of all malignancies,[1] including but not limited to breast, gastric, ovarian, and lung cancer.[2] Its overexpression is associated with aggressive tumor types and poor prognosis in cancer patients. As a result, ErbB2 has become a crucial biomarker for cancer diagnosis and a valuable therapeutic target.[3] Although conventional anti-HER2-based therapies have shown clinical success, there are several drawbacks, including limited drug accessibility to the tumor site, higher therapeutic doses, nonspecific targeting, uneven biodistribution, and unwanted side effects.[4] These challenges reduce the overall therapeutic efficacy of current treatment strategies, underscoring the urgent need for more effective and targeted approaches. Nanotechnology holds enormous potential in addressing these limitations by enabling precision drug delivery and improved therapeutic outcomes.

Recent advances have focused on engineering nanomedicines with unique properties and characteristics for the diagnosis and treatment of ErbB2 cancer.[5] These nanocarriers can selectively deliver therapeutic agents to tumor cells, thereby circumventing the limitations of conventional cancer therapies.[6] Among the emerging nanomaterials, ionic liquids (ILs) are promising molecules in cancer drug delivery due to their unique emulsifying and potentially biocompatible properties.[7] As a result, ILs were used to prepare biocompatible nanoparticles for enhancing drug loading, release, and targeting.[8] They are versatile materials with distinct physicochemical properties, including nonvolatility, structural tunability, tunable solubility, and chemical stability, making them highly advantageous in biomedical applications.[9]

Received: April 26, 2026
Revised: August 7, 2026
Accepted: August 10, 2026

ILs are salts comprising ions associated via weak electrostatic interactions that exist in a liquid state below 100 °C or at room temperature.[10] Owing to their ability to disrupt pathogenic membranes and organelles, several types of ILs, including imidazolium and pyridinium cations, have demonstrated their potential anticancer effects against various cancers.[11,12] However, the reported anticancer ILs possess cationic components like imidazolium are known to be cytotoxic to normal cells, causing detrimental side effects, such as nephrotoxicity, neurotoxicity, and primary biliary cholangitis,[13] thereby raising concerns about their biocompatibility. Consequently, developing ILs that can exert selective toxicity on cancer cells while sparing healthy cells is crucial for advancing targeted cancer therapy and improving therapeutic efficacy. This limitation can be addressed by developing an IL composed of a naturally derived amino acid cation with proven cytocompatibility, like L-proline, to achieve a biocompatible and selective targeting system.[14] Further, the customized nature of ILs allows task-specificity, which has been exploited in this research to synthesize SAILs as nanocarriers for the TM peptide region of ErbB2.

SAILs are a class of ionic surfactants, which can be tailored through careful selection and structural modification of cation or anion components. Under specific conditions, they self-assemble into colloidal nanostructures, such as micelles/vesicles of various shapes and sizes,[15] allowing for encapsulation and delivery of drugs.[16] These nanostructures protect drugs from degradation and facilitate their efficient release at the desired site of action. Recent research has explored self-assembling SAILs for the stable delivery of protein/peptide.[17] SAILs have also shown anticancer potential, with azolium cation-based SAILs demonstrating efficacy against C6 glioma tumor cells, though with limited selectivity.[18] So far, IL-based nanocarriers for targeting ErbB2 cancers have not yet been established, which presents a new avenue through this research where the synergic anti-cancer action of SAIL nanocarriers and the TM peptide region of ErbB2 receptor has been investigated.

In ErbB2-overexpressed cancer cells, the ErbB2 receptor is activated through dimerization with itself or other members of the ErbB2 family (HER1/EGFR, HER3, or HER4), triggering downstream signaling pathways, such as the mitogen-activated protein kinase (MAPK) and phosphatidylinositol 3-kinase (PI3K)/Akt pathways, promoting cell proliferation and survival (Figure S1).[19] Several approaches have been explored to target ErbB2, particularly in breast cancer, by inhibiting its dimerization and subsequent signaling, using antibodies, antibody drug conjugates, and tyrosine kinase inhibitors.[20] However, their therapeutic efficacy is limited due to factors, such as poor distribution in solid tumors, off-target effects on healthy cells expressing ErbB2, and immune reactions that can negatively impact patients.[21,22]

Peptides offer a promising alternative for targeting cancer. Peptide sequences derived from the TM region of the ErbB2 receptor have been evaluated in several studies for their ability to treat ErbB2-positive cancer cells.[20,23,24] These synthetic TM peptides mimic the receptor's TM region and act as competitors that sterically hinder dimerization of the receptor's TM subunits, thereby inhibiting the intracellular signaling cascade.[25−27] This supports the idea that TM domains play a key role in ErbB2 receptor activation and contribute to the anticancer and immunostimulatory properties of the receptor.[28,29] However, the hydrophobic nature of TM peptides presents challenges in peptide design and synthesis.[26−27,30−34] In our previous studies, we identified ILs as an effective means to solubilize highly hydrophobic peptides, enabling bioconjugation and other modifications.[30−33] Along this line, we hypothesized that the TM peptide could function as a targeting moiety for the SAIL nanocarriers.

In this study, we combined the SAIL nanocarrier with a targeting TM peptide for cancer treatment and delivery. A rational and straightforward design was utilized to prepare a suitable delivery system for selective targeting and treatment of HER2-positive cancer by developing a SAIL-based delivery system, endowed with an ErbB2-derived TM peptide as a targeting moiety. Specifically, we designed and synthesized two new SAILs using prolinium as the cationic component. The SAILs formed colloidally stable micelles/vesicles in aqueous buffer solutions above their critical aggregation concentration (cac) at physiological pH. The nanostructure and physical properties of SAILs were characterized by dynamic light scattering (DLS), isothermal titration calorimetry (ITC), and cryogenic transmission electron microscopy (cryo-TEM). Furthermore, the SAIL nanocarrier combined with the ErbB2-derived TM peptide demonstrated selective targeting and synergistic anticancer effect toward ErbB2-positive cancer cells. The anticancer effect was achieved via a dual mechanistic pathway: (1) through the disruption of the cell membrane by SAIL nanocarrier and (2) by suppressing ErbB2-dependent signaling by the TM peptide (Figure 1).

■ RESULTS AND DISCUSSION

Synthesis and Characterization of Surface-Active Ionic Liquids

SAILs were designed and synthesized as nanocarriers for the purpose of target delivery and treatment in cancer. Since amino acids are naturally occurring building blocks, they are biocompatible and biodegradable. Therefore, the amino acid, L-proline, was selected as the cationic component of the SAIL nanoformulation.[35] The SAILs were synthesized by esterification of L-proline to obtain mono-amphiphilic (**MAIL**) or [ProC$_{10}$][Cl] nanocarrier, followed by metathesis of the cation with sodium lauryl sulfate (SLS) anion to obtain bi-amphiphilic (**BAIL**) or [ProC$_{10}$][LS] nanocarrier (Figure 2).[36,37] The structure and purity of both SAILs were confirmed by ^{1}H and ^{13}C NMR (Figures S2–S5), evaporative light scattering detection (ELSD) and high-resolution mass spectrometry (HR-MS) (Table S1 and Figure S6). Differential scanning calorimetry (DSC) analysis confirmed the liquid nature of the synthesized SAILs (T_m = −14.5 °C for **MAIL** and 5 °C for **BAIL**) (Figure S7).

The thermodynamics of aggregation of SAILs in phosphate buffer (PB) (10 mM, pH 7.4) was analyzed using ITC at 37 °C. **MAIL** displayed a two-step endothermic aggregation behavior (ΔH_{cac1} = 1.63 kJ mol^{-1}, and ΔH_{cac2} = 0.61 kJ mol^{-1}) with cac1 and cac2 of 150 μM and 260 μM, respectively (Figure 3a and Table S2). In contrast, **BAIL** displayed exothermic aggregation behavior (ΔH_{cac} = −21.2 kJ mol^{-1}) with a cac of 52 μM (Figure 3e and Table S2). The cac of **MAIL** was higher than **BAIL** due to the higher hydration of Cl^{-} anion compared to lauryl sulfate in the buffer; thus, it decreases its counterion binding to delay the aggregation.[38]

SAILs spontaneously formed self-assembled structures in aqueous buffer solutions above their cac.[16] To gain an insight

https://doi.org/10.1021/acsami.6c08450
ACS Appl. Mater. Interfaces XXXX, XXX, XXX−XXX

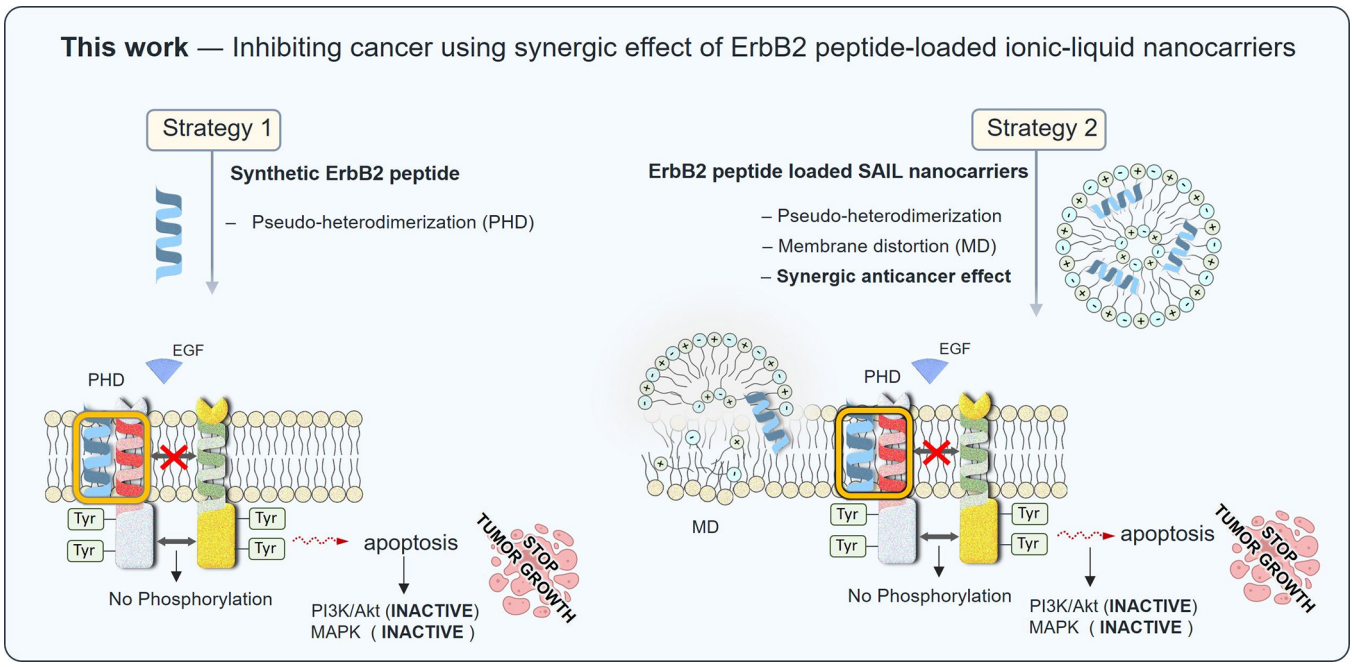

Figure 1. Graphical representation of the proposed mechanism of target delivery and synergistic anticancer activity of SAIL nanocarrier loaded with TM peptide formulation, indicating membrane disruption and damage by SAIL nanocarriers and suppressing ErbB2-dependent signaling, leading to cell lysis and, ultimately, cell death. EGF = Epidermal growth factor.

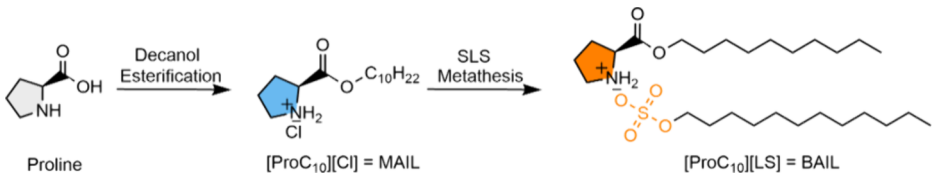

Figure 2. Synthetic scheme of $[ProC_{10}][Cl]$ (**MAIL**) and $[ProC_{10}][LS]$ (**BAIL**).

into the size, morphology, and colloidal stability of the self-assembled **MAIL** and **BAIL** structures, DLS, zeta potential measurements, and cryo-TEM were performed. A zeta potential (ζ) of ≥± 30 mV is indicative of good colloidal stability.[39] DLS analysis of **MAIL** (1.27 mM) revealed larger colloidal structures with a hydrodynamic diameter (D_h) of 712 ± 117 nm and ζ potential of –9.72 mV at 37 °C, indicating aggregated structures with low colloidal stability (Figures 3b and S8). In contrast, **BAIL** formed smaller and more stable colloidal structures, with a D_h of 91 ± 30 nm and ζ potential of –41.5 mV in PB at 37 °C (Figures 3f and S8). These results indicate that **BAIL** forms substantially more stable colloidal assemblies than **MAIL** under physiological conditions.

The trend observed in DLS was supported by cryo-TEM imaging (Figure S9), where **MAIL** formed individual micellar structures with a diameter below 200 nm, along with aggregated micelles with ribbon-like structures (Figure 3c,d). This morphology is attributed to the structural arrangement of mono-amphiphilic prolinium with chloride counterion in the solution. Such structures were reported previously for mono-amphiphilic surfactants under specific conditions.[40] The **BAIL** formed spherical bilayer vesicles with a diameter below 100 nm due to the co-assembly of its amphiphilic constituents (cation and anion) via hydrophobic association, further supported by weak electrostatic interactions of the head-groups (Figure 3g,h). The particle size of **BAIL** nanocarrier, which is below 200 nm, is considered the optimum size for prolonged systemic circulation and passive accumulation in solid tumors via the enhanced permeability and retention effect,[41] implying that **BAIL** can be used as a potential nanocarrier for drug delivery to primary and metastatic tumor sites. The cryo-TEM imaging of the **BAIL**-peptide nanoformulation showed no significant change in the morphological shape or size of **BAIL** nanocarrier due to the incorporation of the peptide (Figure S9e). Due to peptide's small size <50 aa typically displaying widths around 5 nm, they are difficult to be seen under the current settings in cryo-TEM.[42] Cryo-TEM imaging of **V3-BAIL** further showed both individual and fused vesicle structures (Figure S9e). The DLS analysis was in agreement with our cryo-TEM results and showed that compared to the peptide-free **BAIL** nanocarrier, incorporation of the ErbB2 TM peptides **V1**, **V2**, and **V3** did not alter the size of the vesicles (Figure S8c,f–h). However, in both **V1-BAIL** and **V2-BAIL**, the main population shifted toward larger diameters, with a broad maximum centered at approximately 255 nm, but a smaller population around 91 nm was still observed. This behavior may reflect peptide-induced changes in vesicle organization, including partial vesicle association or fusion. In contrast, **V3-BAIL** displayed a predominantly monomodal distribution with D_h of approximately 91 nm (Figure S8h),

https://doi.org/10.1021/acsami.6c08450
ACS Appl. Mater. Interfaces XXXX, XXX, XXX–XXX

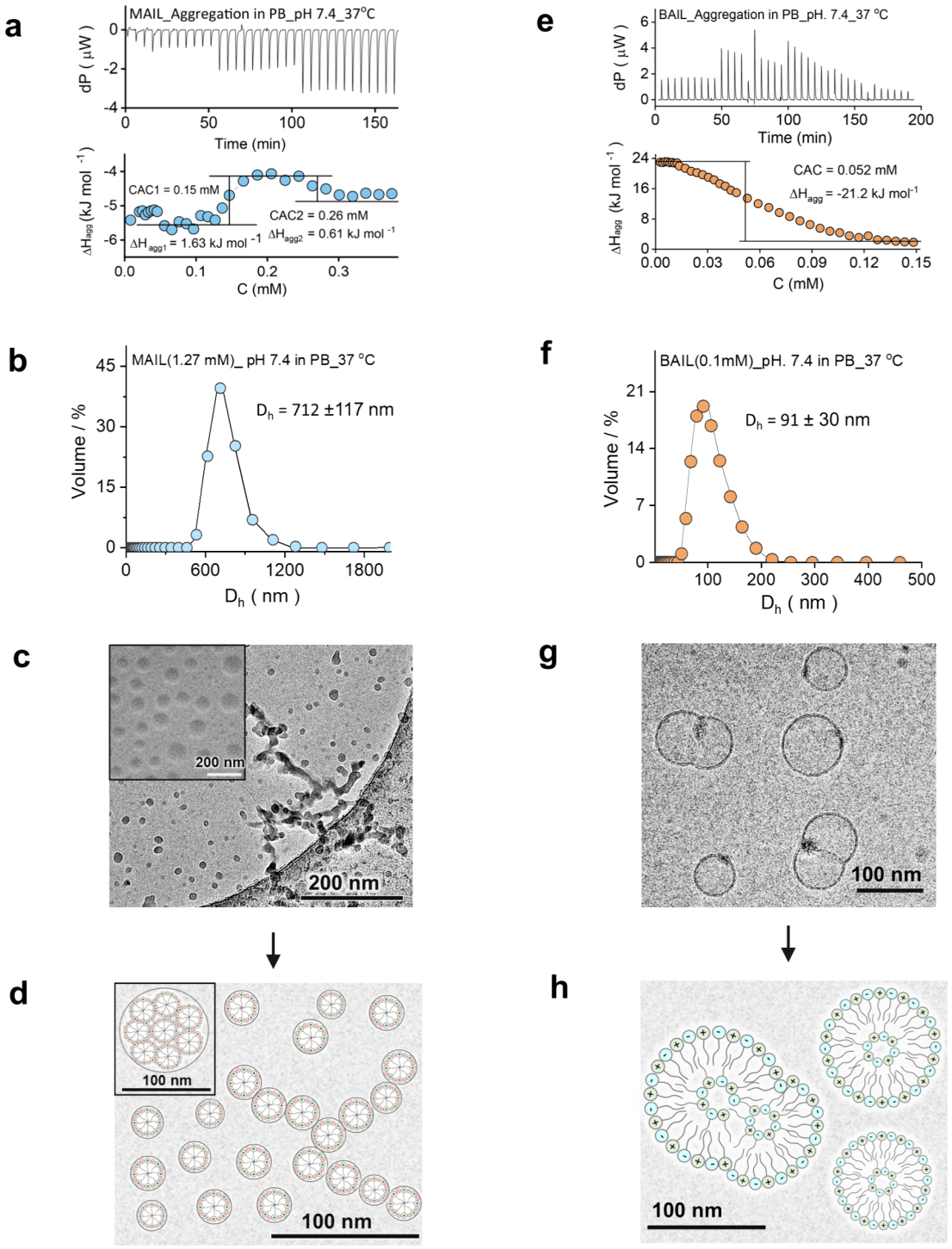

Figure 3. Aggregation characteristics of SAILs in PB pH 7.4. (a–d) **MAIL** and (e–h) **BAIL**. (a, e) ITC curves showing thermodynamics of aggregation at 37 °C. (b, f) DLS profiles. (c,g) Cryo-TEM images and (d, h) cartoon illustration of the cryo-TEM images.

indicating a more homogeneous vesicle population. In agreement with this, the autocorrelation functions displayed smooth decays, without pronounced secondary components, supporting good sample quality for DLS measurement. Together, these data indicate the successful formation of peptide-loaded **BAIL** nanocarriers (Figures S8f–h and S9e).

Additionally, we also evaluated the membrane-forming properties of the SAILs in PB by planar bilayer electrophysiology experiments using bilayer capacitance as a readout of membrane formation quality (see Experimental section). As a reference, 1,2-diphytanoyl-*sn*-glycero-3-phosphocholine (DPhPC) formed a stable planar bilayer with a capacitance of 12.4 ± 2.0 pF (Figure S10).[43] The **BAIL** nanocarrier gave a capacitance of 11.8 ± 0.9 pF, which is comparable to that of the DPhPC and supports the formation of a stable bilayer-like membrane. In contrast, the **MAIL** nanocarrier showed a much lower

https://doi.org/10.1021/acsami.6c08450
ACS Appl. Mater. Interfaces XXXX, XXX, XXX–XXX

capacitance of 3.3 ± 0.5 pF, indicating markedly different membrane-forming behavior and suggesting that **MAIL** does not form planar bilayers of similar quality. This is consistent with the DLS and cryo-TEM data, which together confirm that **BAIL** forms vesicular bilayer assemblies, whereas **MAIL** is likely to adopt micellar monolayer structures (Figures 3c,d,g,h and S10).

Synthesis and Characterization of ErbB2-derived Transmembrane Peptide

To obtain the ErbB2 peptide that serves as the targeting moiety for the SAIL nanocarrier, we identified the core amino acid sequence of the transmembrane segment of the ErbB2 protein (ErbB2_HUMAN, Uniprot P04626) corresponding to amino acid residues 653–675. This selection was inspired by previous research where peptide sequences derived from the ErbB2 TM domain, such as IISAVVGIL (aa 654–662) and VTFIIATVEGVLLFLILVVVVGILIKRR[27] were demonstrated to suppress ErbB2-dependent signaling. Previously reported hydrophobic TMs exhibiting anticancer activity were synthesized by external companies with no detailed explanation of their synthesis and characterization.[26,27] In some reports, the antiproliferative activity of the TM domains on cancer cell lines was inconsistent; inhibition occurred at lower nanomolar concentrations, while no or very little effect was observed at higher nanomolar concentrations.[26] In another study, the maximum effect at micromolar concentration on cell lines occurred after 48 h treatment with a subsequent decline in activity after 72 h, suggesting transient inhibitory effects.[27] These inconsistent activities are attributable to physicochemical limitations inherent to the peptides. The TM peptide sequence used in our study was identified from the ErbB2 receptor and consisted of 23 amino acids with approximately 69% hydrophobic residues (Table 1). Given that our peptide contains a high content of hydrophobic residues, it belongs to "difficult peptides," which are known to present a challenge in every step of their production: synthesis, analysis, characterization, and biological evaluation.[44−46] Structural modifications were introduced, such as poly-lysines[47] and miniPEG (Ado, amino-3,6-dioxaoctanoic acid),[48] to improve its biological activity and physicochemical properties, and obtain **V1–V3** peptides (Table 1). Additionally, the fluorescence tag 5/6-carboxyfluorescein (FAM) was coupled to the N-terminal of **V2–V3** peptides to allow visualization of the peptide by fluorescence microscopy.

The TM peptides **V1-3** were synthesized on a TentaGel RAM resin using a standard Fmoc-based solid-phase peptide synthesis (SPPS) protocol (see Experimental section). The solubilizing properties of the peptides, using **V2** as a model, were also evaluated to determine the optimal purification and characterization conditions (Table S3). All peptides were purified using reversed-phase high-performance liquid chromatography (RP-HPLC) (Figure S11) and characterized by liquid chromatography mass spectrometry (LC–MS). The molecular weights measured by ESI-MS were consistent with the theoretical molecular weights calculated for each peptide (Figure S12). Coupling of the FAM was confirmed by UV–vis and fluorescence spectroscopy (Figure S13a,c).[49]

Since peptide folding represents an important property in receptor recognition and biological activity.[50] The secondary structures of all synthesized peptides were evaluated in 2,2,2-trifluoroethanol (TFE) (10 μM peptide concentration at 23 °C) by circular dichroism (CD) spectroscopy. All peptides (**V1–V3**) demonstrated a characteristic α-helix with two negative bands at 208 and 222 nm and a positive band at 195 nm (Figure S13b,d and Table S4).[30]

SAILs-TM Peptide Nanoformulation

To construct the SAIL-TM peptide nanoformulation, the fluorescently labeled TM peptides (**V2** and **V3**) were fused with **BAIL** or **MAIL** nanocarrier via the reverse evaporation technique (see Experimental section).[51] The binding kinetics of TM peptide to **BAIL** or **MAIL** colloidal structures in an acetonitrile-buffer mixture were assessed using ITC.[52] The TM peptide showed a two-step binding kinetics to the SAIL micelles/vesicles accompanied by endothermic and exothermic enthalpy changes (Figure S14). The high endothermic (+ve dH) changes in step-1 indicate the hydrophobic association of the peptide with the SAILs vesicles/micelles core region,[53] whereas high exothermic (−ve dH) enthalpy changes in step-2 indicates hydrogen bond interactions[54] of peptides' charged groups with the SAILs' headgroups (prolinium or sulfonate) region.

Further evaluation by confocal laser scanning microscopy (CLSM) revealed a strong green fluorescence signal after the association of **V3** peptide (10 μM) with **BAIL** (100 μM) or **MAIL** (300 μM) (Figure S15a,b). However, fluorescent spots disappeared upon dilution of the samples with 25% glycerol, which reduced the concentration of **BAIL** and **MAIL** below their cac. This slowed the motion of the particles and caused the collapse of the nanocarrier structure (Figure S15d,e). In contrast, a vast number of green fluorescent spots were also observed when diluted in a 25% glycerol ACN/H_2O mixture, which is attributed to the lower solubility of **V3** peptide in this mixture, in comparison to conditions without glycerol, where the same level of contrast was observed for **V3** as the background (Figure S15c,f). These results indicate the fusion of **V3** peptide with **BAIL** and **MAIL** nanocarriers, respectively.

The colloidal stability of the **BAIL** and **V3-BAIL** was evaluated under different conditions by monitoring changes in D_h over time (0–48 h). The analysis was performed for **BAIL** in PB buffer (Figure S16), for **V3-BAIL** in PB (Figure S17), and in cell culture medium (Figure S18). Both **BAIL** and

Table 1. ErbB2 TM Peptide Sequences and Analytical Characterization

peptide	amino acid sequence	calculated mass	experimental mass	mass error (ppm)	t_R^e [min]
ErbB2_TM	SIISAVVGILLVVVLGVVFGILI				
V1	SIISAVVGILLVVVLGVVFGILI-Ado-KKKK[a]	738.2452	738.2360[d]	12	4.7
V2	FAM-SIISAVVGILLVVVLGVVFGILI-Ado-KKKK[b]	827.7572	827.7424[d]	18	4.6
V3	FAM-PEG4-SIISAVVGILLVVVLGVVFGILI-Ado-KKKK[c]	889.5427	889.5450[d]	3	4.8

[a]Ado: amino-3,6-dioxaoctanoic acid. [b]FAM: 5(6)-carboxyfluorescein. [c]PEG(4): amino-4,7,10,13-tetraoxapentadecanoic acid. [d]Mass peaks detected as $[M + 4H]^{4+}$. [e]Retention time (t_R) based on 214 nm detection.

https://doi.org/10.1021/acsami.6c08450
ACS Appl. Mater. Interfaces XXXX, XXX, XXX−XXX

V3-BAIL showed only minor changes in D_h when stored in PB at 25 °C, indicating a good colloidal stability and a dominant population centered around the 100–200 nm range under these conditions. The corresponding autocorrelation functions remained well-defined, indicating preservation of the principal diffusing species. Only a minor peak broadening and a limited contribution from larger scattering entities were observed at the later time points, considering minimal formation of higher-order aggregates or vesicular assemblies.

In contrast, storage at 4 °C resulted in a pronounced increase in the particle size, suggesting reduced colloidal stability at lower temperature. This behavior may be related to the thermal properties of **BAIL**, as DSC analysis showed a transition temperature close to 4 °C (Figure S7). Therefore, storage above this transition temperature appears preferable for maintaining colloidal stability of the **BAIL**-based nanoformulations.

In culture medium consisting of RPMI-1640 supplemented with 10% fetal bovine serum (FBS), D_h of **V3-BAIL** at 37 °C was assessed. The medium control exhibited two scattering populations below 100 nm, which are attributed to serum proteins and nanoscale components present in the culture medium. These background features were also present in the **V3-BAIL** samples and were, therefore, not interpreted as evidence of nanoformulation instability. In addition to these medium-derived signals, **V3-BAIL** displayed a distinct population around 200–300 nm, corresponding to the peptide-loaded nanocarriers. This population persisted over 48 h, with only a modest increase in apparent D_h and slight peak broadening. The corresponding autocorrelation functions showed gradual changes but remained well-defined, supporting the continued presence of a dominant diffusing species. A minor contribution from larger scattering entities was observed from 48 h, indicating limited aggregate formation starting at this time. Overall, these results show that **V3-BAIL** is stable as a nanocarrier under cell-culture conditions during the biological assay time scale.

The association of FAM-labeled **V3** with **BAIL** vesicles was estimated using a centrifugation-based separation assay. In the absence of **V3**, **BAIL** showed no absorbance at 495 nm before and after centrifugation, confirming low background signal from the carrier itself (Figure S19). In contrast, **V3-BAIL** nanoformulation showed a strong FAM signal before centrifugation, whereas the signal remaining in the supernatant after centrifugation was markedly reduced. This indicates that a substantial fraction of **V3** was associated with **BAIL** nanocarriers. The DLS data further showed that **V3-BAIL** had a larger hydrodynamic diameter before centrifugation than **BAIL** alone, consistent with peptide association and/or peptide-induced changes in vesicle organization. These results support efficient formation of **V3-BAIL** nanocarriers, while this assay indicates the estimate of vesicle-associated peptide and not a direct measure of peptide insertion into the bilayer.

Cancer Cell Lines and Antiproliferative Action of Individual SAILs

In this work, SAILs were primarily engineered as nanocarriers for targeted delivery to ErbB2-positive cancer cells; certain ILs, such as imidazolium and pyridinium, have previously been shown to exhibit inherent anticancer properties. However, their cationic components are of synthetic nature and known to be cytotoxic to normal healthy cells, which causes detrimental side effects, such as nephrotoxicity, neurotoxicity, and primary biliary cholangitis, raising concerns about their biocompatibility.[11] Therefore, we addressed this limitation by developing an IL with a cation derived from a natural amino acid (proline), aiming to improve its biocompatibility. We first investigated whether the SAIL nanocarriers had any influence on the viability of cancer cells. Cancer cell lines were selected based on high *ERBB2* expression levels and substantial *ERBB2*-CRISPR-dependency scores, indicating high sensitivity to CRISPR/Cas9 knockout of *ERBB2*, from publicly available data in the cancer-dependency map (DepMap)[55] (Table S5 and Figure S20).

Five cancer cell lines were studied to evaluate targeting properties of the SAIL nanocarriers: BT474 and AU565 (breast cancer), A549 (lung adenocarcinoma), CFPAC-1 (pancreatic cancer), and NCl-H23 (lung carcinoma). Among these, AU565 and BT474 exhibit the highest *ERBB2* RNA expression levels (11.6 and 10.5, respectively) together with strong CRISPR dependency scores (both approximately −1.09), indicating a pronounced dependence on ErbB2 signaling. CFPAC-1 and A549 showed moderately elevated *ERBB2* RNA expression levels (5.3 and 4.7, respectively) and substantial CRISPR-dependency scores (−0.7 and −0.78, respectively), consistent with intermediate ErbB2 dependence. In contrast, NCl-H23 cells were included as a low-ErbB2-expression control, based on its markedly lower *ERBB2* RNA level (3.24) and weak CRISPR-dependency score (−0.15). Together, these data defined a panel of cancer cell lines spanning high, intermediate, and low ErbB2 dependence, providing a suitable system to assess the selectivity and targeting performance of the SAIL nanocarriers.

In the in vitro cytotoxicity study, **MAIL** (150 and 210 μM) and **BAIL** (54 and 64 μM) nanocarriers showed no significant reduction in the viability of cancer cells following 24 h incubation (**BAIL**; Figure 4e,f, **MAIL**; Figure 4g,h). Therefore, the experiment was extended further to 48 h. After 48 h incubation, **BAIL** nanocarrier within the concentration range of 52–104 μM exhibited a significant antiproliferative effect on all tested cell lines except AU565 cells (Figure 4a), and the cell viability decreased in a concentration-dependent manner (Figure S21). For instance, the **BAIL** nanocarrier at a concentration of 104 μM significantly reduced the cell viability to 19, 37, and 44% in A549, BT474, and CFPAC-1 cell lines, respectively. The calculated half-maximal inhibitory concentrations (IC_{50}) of **BAIL** were 68.7, 82.3, 121.4, and 264.4 μM against BT474, A549, CFPAC-1, and AU565 cancer cells (calculated for 48 h post-treatment). In contrast, no cytotoxicity toward cancer cell lines was observed after treatment with **MAIL** nanocarrier within the concentration range of 150–300 μM. The structural differences between **MAIL** and **BAIL** play a key role in their cytotoxicity. The inclusion of lauryl sulfate as the anion and the additional alkyl chain in the **BAIL** structure enhances its lipophilicity and increases affinity for cell membranes. As a result, **BAIL** integrates more easily into membranes, destabilizing their structural integrity and inducing toxicity in the malignant cells. These findings align with prior studies that identified the anion type and alkyl chain length as critical determinants of IL toxicity.[56] Previous reports have shown that SAILs induce concentration-dependent effects on membranes, such as rigidification, fluidization, or rupture.[44] Additionally, ILs are known to increase membrane permeability and disrupt physiological barriers, thereby facilitating drug transport to target sites.[8] Membrane damage remains the primary mechanism of IL-induced toxicity.[56,57]

https://doi.org/10.1021/acsami.6c08450
ACS Appl. Mater. Interfaces XXXX, XXX, XXX–XXX

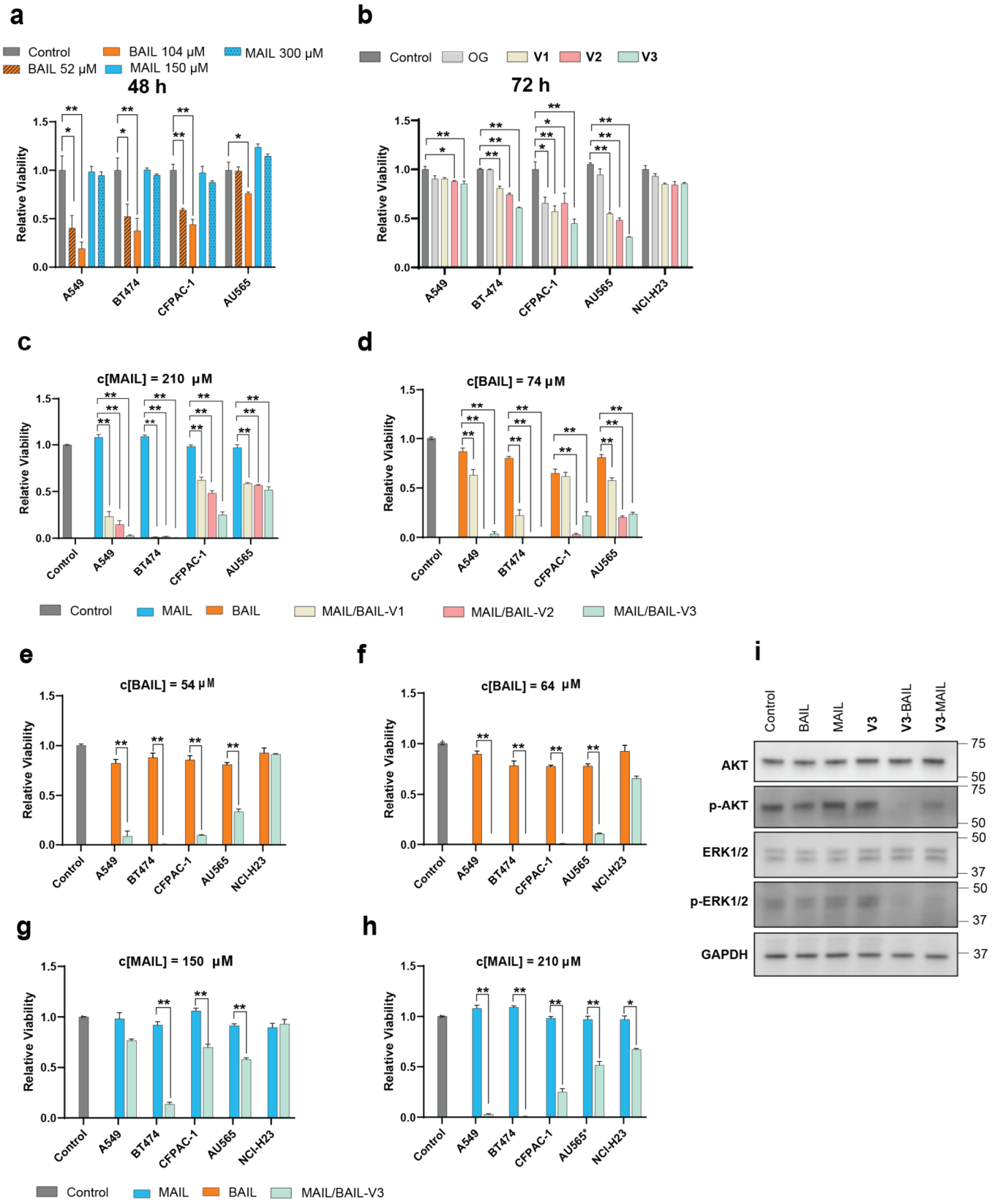

Figure 4. Anti-proliferative activity and cellular mechanism of SAIL-TM peptide nanocarriers. (a) Cell viability of cancer cells following incubation with **BAIL** or **MAIL** alone over 48 h. (b) Viability of cancer cell lines following incubation with TM peptides at a concentration of 1.25 μM for 72 h. (c, d) Viability of cancer cells indicated by the *x*-axis after 24 h incubation with peptides **V1**, **V2**, and **V3** (at concentration 1.25 μM) with either **MAIL** (210 μM) or **BAIL** (74 μM). (e, f) Viability of cancer cells after 24 h incubation with **BAIL** (54 or 74 μM) alone or combined with peptide **V3** (at concentration 1.25 μM) (g, h), as well as **MAIL** (150 or 210 μM) alone or with **V3** peptide. (i) Western blot analysis of the inactivation of the ErbB2 downstream MAPK and PI3K signaling pathway following 2 h incubation of BT474 cells with **V3** peptide-fused **MAIL** or **BAIL**. Values are expressed as mean ± SD ($n = 3$). *P*-values were determined using one-way ANOVA $^{*}p < 0.05$, $^{**}p < 0.01$.

https://doi.org/10.1021/acsami.6c08450
ACS Appl. Mater. Interfaces XXXX, XXX, XXX–XXX

Antiproliferative Action of TM Peptides V1–V3

In the next step, we evaluated the antiproliferative activity, effects on downstream PI3K/Akt and MAPK signaling, and cellular localization of **V1–**V3. Because of the limited aqueous solubility of these hydrophobic peptides, *n*-octyl-beta-D-glucopyranoside (OG) was used to assist solubilization. An OG concentration sufficient to dissolve the peptides without causing cytotoxicity in the tested cell lines was first established and used for later experiments (Figure 4b).

Initial viability studies showed that incubation cells with **V1–V3** at 500 nM resulted in no clear reduction in cell viability after 24–48 h (Figure S22a), and only a minor effect was detected after 72 h (Figure S22b). Increasing peptide concentration to 1.25 μM resulted in a more pronounced effect across the cell lines (Figure S22c). Based on these observations, subsequent experiments were performed at 1.25 μM with an incubation time of 72 h (except for A549 cells, which grow more slower than other cell lines in the panel).

Under these conditions, all three peptides (**V1–3**) reduced cell viability of the tested cell lines panel (Figure 4b). Dose–response analysis further showed that the peptides decreased cell viability in a concentration-dependent manner over the range 0.04–1.25 μM (Figure S23), supporting the selection of 1.25 μM for further studies. Among the three variants, **V3** displayed the strongest antiproliferative effect, reducing viability to 31–61%, whereas **V1** and **V2** were less active and left 55–90% viable cells, depending on the cell line (Table S6). The enhanced activity of V3 is likely related to the presence of the PEG unit, which improves peptide solubility.[58]

Importantly, the magnitude of the antiproliferative effect correlated with ErbB2 expression level in cell lines. Stronger inhibition of viability was observed in the ErbB2-high cell lines AU565, CFPAC-1, and BT474, whereas only negligible effects were detected in A549 and NCl-H23, which show the lowest ErbB2 expression in the panel (Figure 4b). This pattern supports the notion that the TM peptides act in an ErbB2-dependent manner.

Synergistic Antiproliferative Effect of SAILs-TM Peptide Nanoformulation

To generate peptide-loaded nanocarriers, the TM peptides **V1**, **V2**, and **V3** were combined with both SAIL systems, **BAIL** and **MAIL**, according to the procedure described in the experimental part. Cell viability analysis revealed a clear nanoformulation-dependent effect, with all three peptide variants (**V1–V3**), showing substantially greater reduction in viability when delivered in **BAIL** than in **MAIL** vesicles (Figure 4c,d). Across A549, BT474, CFPAC-1, and AU565 cells, **BAIL** nanoformulations consistently shifted the dose–response curves to lower concentrations and induced a stronger loss of viability (IC_{50} between 50 and 70 μM), indicating more efficient delivery and/or enhanced biological activity. This difference was particularly pronounced in A549 and BT474 cells, where **BAIL** nanoformulations caused a steep decrease in viability, whereas the corresponding **MAIL** nanoformulations required higher concentrations and generally produced weaker responses (Figure S24). Overall, **V3** showed higher activity than **V2** and **V1**, suggesting that peptide sequence-dependent features further modulate activity once efficient vesicular delivery is achieved. This improved performance may be related to the N-terminal PEG unit in **V3**, which is known to promote cell membrane interactions and fusion-like processes without causing direct biochemical disruption. Such PEG-mediated fusion effects are well-documented, for example, in the fusion of B-cells and myeloma cells during hybridoma formation.[59]

CFPAC-1 cells displayed an intermediate response, whereas AU565 cells were comparatively resistant to **MAIL** but became markedly more sensitive when the peptide was delivered in **BAIL** nanocarriers, further highlighting the importance of the carrier system (Figures 4c–h, S24 and S25). Importantly, the combined SAIL-peptide nanoformulations show an effect toward ErbB2-positive cell lines, with the magnitude of the viability reduction correlating with the level of ErbB2 expression (higher ErbB2 expression was associated with stronger inhibition of viability). Consistent with this, the **V3-BAIL** nanoformulation showed no significant effect on NCl-H23 cells after 24 h, while **V3-MAIL** showed only a minor effect and only at the increased tested **MAIL** concentrations (210 μM). Even under these conditions, the response in NCl-H23 cells maintained clearly weaker than that observed in the ErbB2-positive cancer cell lines (Figure 4e–h).

Chou-Talalay analysis was performed to quantify whether the results of cell viability experiments are caused by SAILs (**BAIL** or **MAIL**) with TM peptides (**V1-3**) synergistic, additive, or antagonistic effect.[60] The analysis was evaluated in BT-474 cells using Compusyn software based on the combination index (CI) method.[61] The compounds were tested in combination at different dose ratios, and the resulting effects were used to calculate CI values. Across the tested dose range, the calculated CI values were consistently well below 1, demonstrating strong pharmacological synergy between the SAIL carriers and TM peptides (Figure S26).

When compared antiproliferative effect of the best-performing **V3-BAIL** nanoformulation with the reference drugs doxorubicin and cisplatin (Figure S27a,b), **V3-BAIL** (Figures 4e,f and S24) showed comparable antiproliferative efficacy in ErbB2-positive cell lines (A549, CFPAC-1, and AU565). However, the absolute effective concentrations differed (~50 μM for **V3-BAIL** vs ~10 μM for cisplatin and ~0.3 μM for doxorubicin. For **V3-BAIL**, this effect was obtained already after 24 h of incubation, whereas the standard drugs were evaluated after 48 h, due to the no visible effect after 24 h. Interestingly, BT-474 cells were more resistant to both doxorubicin and cisplatin, with over 70% of cells remained viable after 48 h, whereas **V3-BAIL** retained strong antiproliferative activity in BT-474 cells within the same concentration range observed for the other ErbB2-positive models. An additional important distinction was the selectivity of the response. In contrast to cisplatin and doxorubicin, which did not discriminate between cell lines based on ErbB2 status and reduced viability in NCl-H23 cells at concentration similar to those effective in ErbB2-positive cells, **V3-BAIL** showed nonsignificant effect in NCl-H23 cells (Figure 4e,f). This selective activity is consistent with the proposed mechanism of action, in which the V3 contributes to receptor-dependent targeting, IL nanocarriers promote membrane interaction and enhance peptide delivery.

Trastuzumab, a clinically established ErbB2-targeting therapy, was also evaluated in the same cell panel (Figure S27c,d). Under the tested conditions, trastuzumab did not show a clear reduction in cell viability across most cell lines and did not show an obvious dependence on ErbB2 expression level, either after 48 h or 150 h of treatment. Only BT-474 cells showed a noticeable reduction in viability after 150 h (Figure S27d). In parallel,

https://doi.org/10.1021/acsami.6c08450
ACS Appl. Mater. Interfaces XXXX, XXX, XXX–XXX

trastuzumab reduced confluency in BT-474 cells but did not affect confluency in ErbB2-negative NCl-H23 cells, indicating an ErbB2-dependent mode of action (Figure S28a–c). Importantly, **V3-BAIL** showed a complete reduction in viability at around 50 μM concentration in BT-474 cells over 24 h (Figure S25), indicating that this **V3-BAIL** is both more potent and more selective in ErbB2-positive models under the conditions tested.

To gain mechanistic insights into the strong antiproliferative activity of the **V3-BAIL** nanoformulation, we examined its effect on ErbB2-dependent downstream signaling (Figure 4i). Western blot analysis revealed that **MAIL** and **V3** peptide alone had little to no effect on signaling, while **BAIL** alone caused only a modest decrease in AKT and ERK 1/2 phosphorylation. In contrast, the combination nanoformulations, **V3-BAIL** and, to a lesser extent, **V3-MAIL**, strongly suppressed both the PI3K/Akt and MAPK signaling pathways, as shown by the reduced levels of phosphorylated AKT and phosphorylated ERK1/2 (Figures 4i and S29). This clear signaling inhibition is consistent with the cell viability data and Chou-Talalay synergy analysis, supporting a synergistic mechanism between the SAILs nanocarrier and the ErbB2-delivered TM peptide.

To gain understanding of nanocarrier uptake and the cellular response to the **V3-BAIL** nanoformulation, we performed mechanistic studies using brightfield imaging, confluency analysis, and propidium iodide (PI) uptake measurements (Figure 5). The results show that **V3-BAIL** induced a clear loss of cell fitness (Figure 5a), while causing only minimal additional PI uptake compared with controls (Figure 5b). Morphologically, treated cells became progressively rounder and detached over time (Figure 5a), while remaining largely PI-negative, indicating that **V3-BAIL** does not primarily induce rapid plasma membrane rupture but instead triggers an early stress-associated or pre-lytic death phenotype. In parallel, the increasing GFP-associated signal (Figure 5c) confirmed intracellular accumulation of **V3-BAIL** over the course of the experiment. Notably, overall confluency increased similarly in treated and control cultures (Figure 5d), suggesting that the treatment effect was not simply reflected by a total reduction in surface coverage within the imaging window. Together with the live-cell imaging data (Figure S30), the observations support a mechanism in which **V3-BAIL** is taken up by the cells and impairs viability through intracellular and membrane-associated stress rather than through lytic disruption.

To further examine the interaction of **V3-BAIL** nanoformulation with lipid membranes, we performed planar lipid bilayer electrophysiology experiments using DPhPC as a mimic of biological membrane (Figure S10e–i). The addition of **V3-BAIL** to the DPhPC lipid bilayer led to a clear initial fluctuation of the current, followed by stabilization of the membrane current, indicating direct interaction of **V3-BAIL** with the bilayer. This behavior was accompanied by a significant drop in bilayer resistance, from 35.41 GΩ to 1.80 GΩ at −50 mV and from 33.87 GΩ to 1.15 GΩ at +50 mV, corresponding to an approximately 20-fold and 30-fold decrease, respectively (Table S7). The capacitance changed modestly, decreasing from 23.83 pF to 22.00 pF at −50 mV and from 28.02 pF to 27.07 pF at +50 mV. Together, these data indicate that the **V3-BAIL** nanoformulation produced a strong increase in bilayer conductance and substantial membrane perturbation, while the relatively

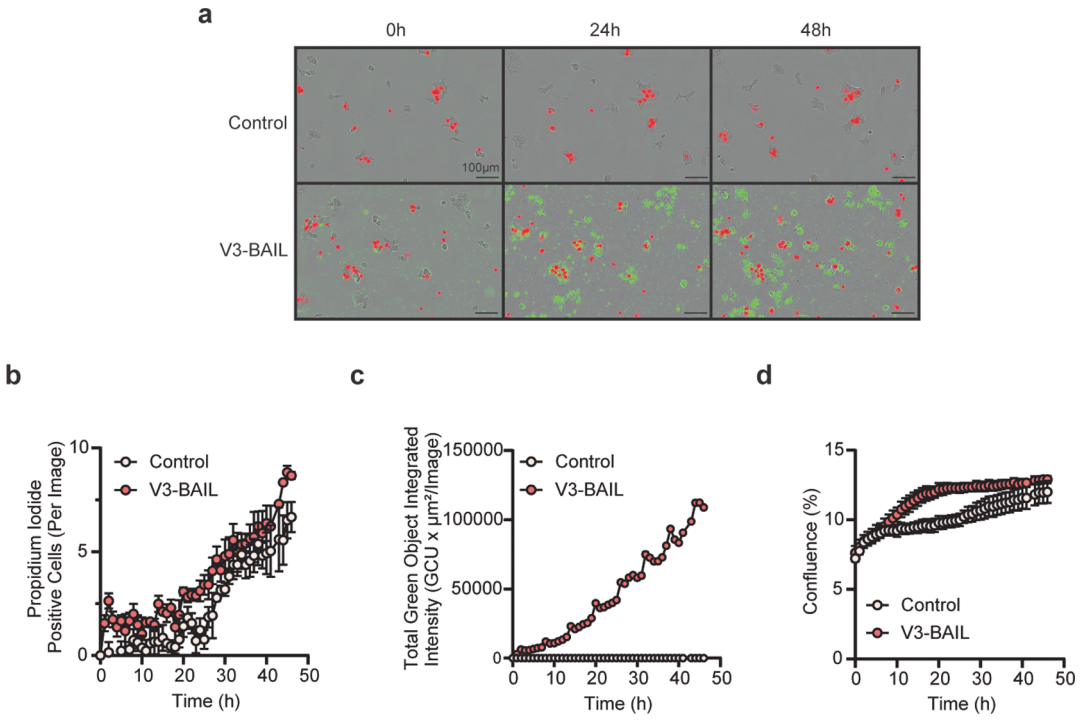

Figure 5. (a) Representative images of BT-474 cells untreated (upper) or incubated with fluorescently labeled **V3** peptide (green) in combination with **BAIL** nanocarriers (bottom) (**V3**: 1.25 μM, **BAIL**: 54 μM). Magnification: 4×. Scale bar = 100 μm. (b) Quantification of BT-474 propidium iodide-positive cells in untreated conditions or treated with **V3-BAIL** (**V3**: 1.25 μM, **BAIL**: 54 μM). (c) Total green object integrated intensity quantification over time of BT-474 cells in untreated condition or treated with **V3-BAIL** (**V3**: 1.25 μM, **BAIL**: 54 μM). (d) Confluency of BT-474 cells was measured from phase contrast images at different time points and was plotted as mean confluency (%) vs time for untreated and **V3-BAIL** (**V3**: 1.25 μM, **BAIL**: 54 μM) treated cells.

https://doi.org/10.1021/acsami.6c08450
ACS Appl. Mater. Interfaces XXXX, XXX, XXX–XXX

limited change in capacitance argues against membrane rupture. Thus, within this model membrane system, our nanoformulation exhibited stronger membrane activity than any individual component or carrier control. (Figure S10i). Together with the low PI uptake observed in cells (Figure 5), this supports an interaction model, where **V3-BAIL** has a controlled membrane-active effect that may facilitate cellular interaction and delivery without triggering lytic damage.

■ CONCLUSIONS

In conclusion, our data identified **V3-BAIL** as a selective dual-action nanoformulation for targeting ErbB2-positive cancer cells. The **BAIL** nanocarrier substantially improved the activity of the hydrophobic **V3** transmembrane peptide, most likely by enhancing its membrane association and cellular uptake, whereas the free peptide also showed only limited activity under comparable conditions. Mechanistically, **V3-BAIL** did not act through rapid nonspecific membrane lysis but rather induced a progressive loss of cellular fitness accompanied by cell rounding and detachment, with minimal propidium iodide uptake. At the molecular level, this effect was associated with strong suppression of the PI3K/Ark and MAPK/ERK signaling pathways, supporting the conclusion that the **V3** peptide functionally interferes with ErbB2-dependent signaling once efficiently delivered by the **BAIL** nanocarrier. Interestingly, the activity of **V3-BAIL** correlated with ErbB2 expression level, showing a strong effect in ErbB2-positive cell lines and minimal effect in low-ErbB2 cells, which resulted in a clear contrast to conventional chemotherapeutics such as doxorubicin and cisplatin, which did not discriminate between cell lines based on ErbB2 status. Moreover, under the tested conditions, **V3-BAIL** displayed more rapid and pronounced activity than trastuzumab. Together, these findings demonstrate that **V3-BAIL** combines carrier-driven delivery, membrane-associated cellular entry, and receptor-dependent signaling inhibition to achieve synergistic and selective anticancer activity, highlighting its promise as a new strategy for ErbB2-targeted therapy.

■ EXPERIMENTAL PART

Synthesis of TM Peptides

The amino acid sequence of the hydrophobic TM fragment was derived from the human receptor tyrosine-protein kinase (ErbB2_HUMAN, Uniprot P04626) (aa. 653–675). TM peptides were synthesized on a TentaGel RAM resin with a loading capacity of 0.21 mmol/g using SPPS, which consisted of an automated reaction using Intavis MultiPep CF peptide synthesizer and manual reaction in a vessel. In the automated synthesis, amino acid couplings were carried out with the molar ratio of (5):(5):(10) of (Fmoc-protected amino acid):(HBTU):(NMM) at room temperature for 30 min. Deprotection was achieved by treating the resin with 20% (v/v) piperidine in dimethylformamide (DMF) for 5 min, 15 min, respectively, at room temperature. Additional 0.3 mL of NMP was added during each coupling cycle to enhance the synthesis. Peptide-bound resin was capped with 5% (v/v) acetic anhydride in DMF for 5 min. In the manual reaction, coupling of 5(6)-FAM and Fmoc-PEG4-OH (PEG4) to the peptide-bound resin was carried out with the molar ratio of (4):(4):(8) of (FAM or PEG4):(HBTU):(*N,N*-diisopropylethylamine, DIPEA) at room temperature for 120 min and repeated one time, except for the first coupling cycle of Fmoc-PEG4-OH which was done overnight. Deprotection was achieved in 20% (v/v) piperidine in DMF for 5 min, 15 min, respectively, at room temperature. After the coupling and deprotection step, DMF washing was performed. In the final N-terminal Fmoc deprotection, the resin was first washed with dichloromethane (DCM), followed by washing with DMF. The peptide-bound resin was dried before cleavage. The peptide was cleaved from the resin using a cleavage cocktail consisting of 95% pre-dissociated trifluoroacetic acid (TFA) mixed with reagent K: (TFA/phenol/Milli-Q water/thioanisole/1,2-ethanedithiol, (82.5:5:5:5:2.5% v/v)),[62] and the mixture was shaken at room temperature for 3 h. The crude peptides were precipitated in cold diethyl ether, centrifuged, and the resulting pellet was washed three times with diethyl ether. The peptides were solubilized in an acetonitrile (ACN)/Milli-Q water solution and lyophilized to obtain the crude peptide.

Characterization of TM Peptides

Reversed-Phase High-Performance Liquid Chromatography (RP-HPLC Analysis). All peptides were analyzed by analytical RP-HPLC on a Waters 2695 Alliance system (Waters, Milford, MA, USA) equipped with a Waters 2998 photodiode array (PDA) detector. HPLC eluent A was Milli-Q water (0.1% TFA), and eluent B was ACN (0.1% TFA). HPLC conditions are specified for each experiment separately. ISERA C4 (50 × 3.0 mm, 5.0 μm) column was used for the analysis with a flow rate of 2 mL/min. If not stated otherwise, chromatograms were extracted and analyzed at 214 nm. The analysis of TM peptides was achieved using an analytical method that starts with an isocratic elution of 10% B for 4 min, followed by a gradient elution of 40% to 95% B for 6 min.

Preparative HPLC Purification. Purification of the compounds was achieved using a Waters 1525 binary pump equipped with a Waters 2998 PDA detector (Waters, Milford, MA, USA). HPLC eluent A was Milli-Q water (0.1% TFA), and eluent B was ACN (0.1% TFA). The crude peptides were purified using a Multo HighBio 300–5 C4 (250 × 20 mm, 5.0 μm) column. The **V1** crude peptide was first dissolved in a solvent mixture of 35:65% (v/v) ACN/Milli-Q water with 0.1% TFA and purified using an isocratic elution of 10% of B for 10 min followed by a linear gradient of 40 to 95% of B for 40 min at a flow rate of 8 mL/min and detected at 214 nm. Both **V2** and **V3** were dissolved in 50:50% (v/v) ACN/Milli-Q water with 0.1% TFA and purified with a linear gradient of 30% to 95% of eluent B for 40 min at a flow rate of 8 mL/min and detected at 214 and 445 nm.

LC–MS Analysis. The molecular weight of the purified peptides was confirmed by mass spectrometry on a Bruker TOF Q impact II spectrometer (Bruker Daltonik GmbH, Bremen, Germany) and calibrated using a Bruker ESI-Tune-Mix or Waters SYNAPT G2-Si HR-MS spectrometer equipped with a Waters Acquity UPLC system (Waters, Milford, MA, USA). UPLC eluent A was Milli-Q water with 0.1% formic acid (FA), and eluent B was methanol (MeOH) with 0.1% FA. UPLC conditions for the analysis of the peptides started from 50% to 95% of B in 10 min, followed by isocratic 95% B for 5 min at a 0.3 mL/min flow rate using ISERA UPLC C4 (50 × 3.0 mm, 1.7 μm) column.

Fluorescence Spectroscopy. Steady-state emission and excitation spectra were measured with a spectrofluorometer (FLS1000, Edinburgh Instruments) equipped with a Xe lamp. **V2** and **V3** were prepared at a concentration of 1.4 μM in 25 mM OG (pH 7.9) at 25.1 °C. The fluorescence excitation spectra for **V2** and **V3** were recorded from 280 to 520 nm (emission at 520 nm), and the fluorescence emission spectra were recorded from 490 to 700 nm (excitation at 480 nm).

CD Spectroscopy. CD spectroscopy of samples was performed on a Chirascan applied photophysics in a 1 cm path-length quartz cuvette over a wavelength range of 180–280 nm at 23 °C. Peptides were prepared at a concentration of 10 μM either in TFE or 25 mM aqueous OG (pH 7.9). TFE measurements were taken at a time per point of 1 s and a bandwidth of 1.0 nm with a step size of 1 nm. For each peptide in TFE, three successive scans were recorded as absorbance in mdeg. The same parameters were used for OG samples with the exception that only one run was performed with 10 s time per point to improve the signal-to-noise ratio. CD chromatograms were plotted

https://doi.org/10.1021/acsami.6c08450
ACS Appl. Mater. Interfaces XXXX, XXX, XXX–XXX

with Origin software. For deconvolution analysis, we used the DICHROWEB web server with the CDSSTR algorithm and the SMP180 reference dataset.[63−66]

Synthesis of Surface-Active Ionic Liquids (SAILs)

The first esterification reaction was modified from a previous protocol and performed using thionyl chloride ($SOCl_2$) and a catalytic amount of 4-dimethylaminopyridine (DMAP) to afford **MAIL** nanocarrier represented as [Pro][Cl].[36] In the next step, equimolar amounts of the ester and SLS underwent a metathesis reaction in hot water, which was also modified from a reported protocol, to afford **BAIL** nanocarrier represented as [Pro][LS].[37]

Synthesis of (*S*)-2-((Decyloxy)carbonyl)pyrrolidin-1-ium Chloride (MAIL). L-Proline (772 mg, 6.710 mmol) and Decanol (5.647 mL, 4.68 g, 29.57 mmol) were heated up to 60 °C, producing viscous suspension (B.P. of Decanol 220–235 °C). Thionyl chloride (0.537 mL, 880 mg, 7.40 mmol) was added, followed by DMAP (4 mg, 0.03 mmol). The reaction mixture was stirred at 60 °C for 5 h. Afterward, DCM (20 mL) was added, and the solution was cooled down to 4 °C using ice-cold water. After a dropwise addition of triethylamine (1.591 mL, 1154 mg, 11.41 mmol), a white layer was formed, and the reaction mixture was stirred for an additional 3 h at room temperature, and the layers disappear. Reaction completion was monitored in TLC using 50:50% (v/v) MeOH/DCM (as mobile phase) with $KMNO_4$ stain for visualization of spots. Toluene (20 mL) was added, and the precipitated crude product was filtered off to remove triethyl ammonium chloride salt. The oily residue was purified by Biotage automated column chromatography using 1:1 (v/v) petroleum ether/ethyl acetate to remove the side product and then 20:80% (v/v) MeOH:DCM was to elute the pure target product. The pure product was obtained as a yellow oil 1130 mg (yield; 58%).

Synthesis of (*S*)-2-((Decyloxy)carbonyl)pyrrolidin-1-ium Dodecyl Sulfate Compound (BAIL). To obtain proline decyl ester lauryl sulfate, initially a freshly synthesized ester decanol (50 mg, 0.00017 mmol) was dissolved in 1 M HCl (5.5 mL) for 10 min then additional 30 mL of Milli-Q water was added and mixed for an additional 20 min. Following this, SLS (49 mg, 0.00017 mmol) was dissolved in equimolar amounts at (60 °C), and the reaction was run for 6 h. After the completion of the reaction, water was slowly removed by lyophilization, and a white solid precipitate was collected. The crude solid was dissolved in 30 mL of DCM to extract the pure product from the mixture, and solid sodium chloride was filtered off. The filtrate was washed with Milli-Q water (4 × 30 mL), and the white solid (accounted for NaCl as a by-product) was separated out. Two to three drops of 0.1 M $AgNO_3$ were added to the washings to confirm the presence/absence of chloride ions. The clear but slightly yellow extract was left under vacuum at 0.2 mmHg for 5 h to afford 37 mg, 41% of the pure product as a yellow oil, which crystalized at room temperature.

Characterization of Surface-Active Ionic Liquids (SAILs)

ELSD Analysis. For **MAIL** and **BAIL**, an Agilent Varian 385-ELSD was connected to the HPLC system and used for detection. The analyzed samples were prepared at a concentration of 1 mM in a 1% (v/v) dimethyl sulfoxide/Milli-Q water solution. The ELSD nebulizer and evaporative temperature were set to 50 and 70 °C, respectively, and the gas flow was set to 1.6 SLM. The LC method was performed on an ISERA C18 (50 × 4.6 mm, 3.0 μm) column using a gradient from 10% to 90% of B over 10 min at a flow rate of 2 mL/min.

LC–MS Analysis. The molecular weights of **BAIL** and **MAIL** were confirmed by mass spectrometry on the equipment as described above. UPLC eluent A was Milli-Q water with 0.1% FA, and eluent B was ACN with 0.1% FA. UPLC conditions for the analysis of **BAIL** and **MAIL** were started from 10% to 90% of B in 10 min, followed by isocratic 90% B for 3 min at a 0.3 mL/min flow rate using an ACQUITY UPLC BEH C18 (50 × 2.1 mm, 1.7 μm) column.

NMR Spectroscopy Analysis of the SAILs. Spectra were recorded at the Swedish NMR Centre on a Bruker Avance III HD NMR spectrometer with 800 MHz 1H; 201 MHz 13C magnet at 25 °C. All chemical shifts are reported in parts per million (δ) relative to the residual solvent peak. The following abbreviations are used to denote signal patterns: (s) singlet, (d) doublet, (t) triplet, (q) quartet, (m) multiplet, and (br) broad. Coupling constants (*J*) are reported in Hertz (Hz).

DSC Measurement. DSC traces were obtained using a TGA/DSC 3 + STARe system (METTLER TOLEDO) under N_2 atmosphere. Before performing measurements, samples were completely dried under vacuum for at least 24 h. The scanning rate was 5 °C min^{-1}. Reproducible thermograms of 3rd and 4th cycles were considered for presentation.

ITC Measurement. ITC experiments were carried out using a MicroCal, VP-ITC micro calorimeter with an instrument-controlled Hamilton syringe with a volume capacity of 280 μL at 25 and 37 °C. Titrations were done by adding different aliquots of titrant, i.e. **BAIL** or **MAIL** solution (2–10 μL) into the sample cell containing 1.435 mL of Milli-Q water or PB (10 mM, pH 7.4). Enthalpy changes due to titration into the sample cells were calculated compared to Milli-Q water or buffer solution at the same temperature in the reference cell. The concentration of the sample in the syringe was varied for different experiments. The temperature, time between each injection (300 s), and stirring speed (500 rpm) were controlled with instrument software. The enthalpy change at each injection was measured and plotted against concentration by using Origin software provided with the instrument. The cac was calculated from the inflection point after taking first derivative of the enthalpy vs concentration curve. Since enthalpy is a state function, change in enthalpy due to aggregation (ΔH_{agg}) was calculated by subtracting the constancy in enthalpy before and after aggregation.

DLS and Zeta Potential Measurements. DLS and zeta potential measurements were carried out to determine the size of **BAIL** or **MAIL** colloidal vesicles using Zetasizer Nano ZS (Malvern Instruments, U.K.) with a He–Ne laser (633 nm, 4 mW) as light source at a scattering angle of 173°. Before measurement, solutions were filtered directly into 1 cm path-length sample cell using a membrane filter (0.45 μm). The accuracy of the size measurements was indicated by a correlation coefficient vs time curve.

Planar Bilayer Electrophysiology of the Surface-Active Ionic Liquids. Resistance and capacitance (RC) were estimated using an Orbit Mini miniaturized bilayer recording device (Nanion Technologies, Munich, Germany) equipped with a microelectrode cavity array (MECA 4) recording chip (Ionera Technologies, Freiburg, Germany). A four-well chip with 100 μm cavities was used. The current across each well, $I(t)$, was recorded at a sampling frequency of 1.25 kHz, a bandwidth of 0.625 kHz, and a current range of −2 to +2 nA. All experiments were conducted at room temperature. Each chip well was filled with 150 μL of 50 mM PB (pH 7.4). Stock solutions of DPhPC (4ME 16:0 PC) were prepared in electronic-grade octane and stored at −20 °C. Lipid bilayers were formed over the cavity aperture by the air bubble method, as described previously.[67] Formation of a sealing bilayer was indicated by a negligible current (<0.1 pA), whereas a saturated current signal (±2 nA) indicated the absence of a stable membrane. In cases of unstable current signals or cavity blockage ($C < 1$ pF), the membrane was disrupted using the Zap function and reformed. After bilayer formation, the membrane was allowed to equilibrate for 60 s. RC estimation was then carried out using a predefined voltage protocol consisting of a triangular wave and a seal-test pulse. For the triangular wave, the amplitude (V_{amp}) was set to 100 mV and the period (T_{period}) to 20 ms. For the seal-test pulse, the pulse amplitude (V_{pulse}) was set to 100 mV, the pulse duration (T_{pulse}) to 200 ms, and the holding time (T_{hold}) to 500 ms. Following the initial RC estimation, a constant holding potential of either −50 or +50 mV was applied to assess current stability, and a baseline current was recorded for 120 s. At 180 s, the sample solution was added directly to the chip well to achieve the desired final

https://doi.org/10.1021/acsami.6c08450
ACS Appl. Mater. Interfaces XXXX, XXX, XXX−XXX

concentration, while the current recording was maintained continuously throughout the experiment. After the current reached a stable elevated level, RC estimation was repeated using the same voltage protocol to evaluate membrane stability following sample addition.

Preparation of TM Peptide-SAIL Nanocarriers

A reverse-phase evaporation technique was employed to incorporate the peptide into the carrier as described previously.[51] Peptide stocks of 100 μM were initially made by dissolving the desired amounts of peptide powder in 1,1,1,3,3,3-hexafluoroisopropanol (HFIP). Then, the desired volume of peptide stock solution was mixed with prepared either a **BAIL** (5 mM) or **MAIL** (15 mM) nanocarrier solution in 10 mM PB (pH 7.4, 21 °C) to make secondary stocks. The mixture containing peptide-nanocarrier was left under reduced pressure for the complete evaporation of HFIP and to allow the incorporation of peptides into the carrier.

Electron Microscope Imaging Using Negative Stain

For normal TEM imaging, the SAIL samples were prepared at 1 mM in 10 mM PB (pH 7.4). The samples were then subjected to three freeze-and-thaw cycles and were kept in a warm water bath for 30 min at 37 °C before extrusion. The extrusion was performed 20 times at the transition temperature of the SAILs (**BAIL** T_g = 29 °C, **MAIL** T_g = 10.8 °C) at 37 °C using a 0.1 μM polycarbonate filter. Both the non-extruded and extruded samples were checked by EM using a conventional negative staining protocol. Briefly, a 5 μL sample drop was adsorbed onto a glow-discharged carbon-coated copper CF300-Cu grid type, and the residual solution was blotted off. The grids were discharged under an air atmosphere with negative polarity and 20 mA current for 60 s. The grids were washed twice with 25 μL drops of Milli-Q water and stained twice with 2% uranyl acetate drops. The samples were imaged using a Talos L120C transmission electron microscope (Thermo Fisher Scientific Inc., USA) at a working voltage of 120 keV with a LaB6 filament and a BM-Ceta CMOS detector.

For the cryo-TEM imaging, **BAIL** (15 mM) and **MAIL** (20 mM) were prepared in 10 mM PB (pH 7.4, 19 °C), respectively, and extruded as described previously. Following the extrusion, the samples were vitrified with the aid of the Thermo Fisher Vitrobot Mark IV plunge-freezing system. Briefly, a 3 μL sample drop was adsorbed onto glow-discharged of different grid types, including Quantifoil R1.2/1.3 Cu300, Quantifoil R2/2 Cu300, and carbon type lacey (2–3 nm thickness). The grids were discharged under an air atmosphere with negative polarity and 20 mA current for 60 s. The blot time was 4 s with 30 s holding time, and the residual solution was blotted off. Double blotting was performed as needed to obtain more detailed images. The samples were imaged using a Talos Arctica at a working voltage of 200 keV with an X-FEG filament and Falcon III detector.

Cell Lines and Culture

Human cell lines were acquired from ATCC. All cell lines were regularly tested and were negative for mycoplasma. All cells were cultured in a humidified incubator at 37 °C and 5% CO_2. Cells were maintained in either DMEM (AU565) or RPMI-1640 (A549, CFPAC-1, BT474, NCI-H23) supplemented with 10% FBS and 0.1% gentamicin.

Cell Viability Assay

Stock solutions of peptides were prepared in HFIP. The desired amount was dried and redissolved in 25 mM OG in 10 mM PB (pH 7.4, 21 °C) to obtain 100 μM stocks. For the nanocarrier testing, stock solutions of the SAILs were prepared as 10.4 mM of the **BAIL** and 15 mM of the **MAIL** by dissolving the desired amount in 10 mM PB (pH 7.4, 21 °C). Peptides and nanocarrier stocks were diluted through serial dilution in the corresponding biological buffer media to obtain the final assay concentrations. The tested peptide has a final OG concentration of 0.3 mM. For the peptide-nanocarrier nanoformulations, the stocks were prepared using a reverse-phase evaporation technique as explained in this section. In all cases, the volume of the added dose was kept at <3% of the total volume of the cells-containing media. The cells were plated in a white, opaque 96-well plate with a clear bottom at a density of 5000 cells/well. The incubation time for the peptide, nanocarrier, and peptide–nanocarrier nanoformulation was 72, 48, and 24 h, respectively. For cisplatin and doxorubicin studies, the incubation time was 48 h, for trastuzumab 48 and 120 h. Following incubation, the cell viability was assessed via a CellTiter-Glo Luminescent Cell Viability Assay (Promega #G7570, Madison, Wisconsin).

Live-Cell Imaging

Live-cell imaging was performed using an Incucyte SX5 system (Sartorius) equipped with G/O/NIR optics. Cells were monitored in real time, and green and orange channels were used to visualize fluorescently labeled **V3** peptide in combination with **BAIL** nanocarriers and PI.

Western Blot

Cells were treated with solvent OG control, 1.25 μM of **V3,** or 1.25 μM **V3**-loaded nanocarrier (**MAIL** or **BAIL** at cac) for 2 h. Cells were collected and lysed in RIPA buffer (#89900, Thermo Fisher) with a complete protease and phosphatase inhibitor cocktail (#78440, Fisher Sci). Protein lysates were subsequently heated at 95 °C in Laemmli buffer (#1610737, BioRad) supplemented with β-mercaptoethanol (#M3148, Sigma-Aldrich) for 10 min. Proteins were separated on 4–20% Mini-PROTEAN TGX Stain-Free gel (#4568096, Bio-Rad) and then transferred onto a 0.2 μM nitrocellulose membrane (#1704159, BioRad). The membrane was blocked with 5% BSA bovine serum albumin in TBS-T (#09-7510-100 Fisher Sci) for 1 h with gentle rocking. The membrane was incubated overnight at 4 °C with the following primary antibodies diluted 1:1000: anti-Akt, anti-phospho-Akt, anti-Erk1/2, anti-phospho-Erk1/2, and anti-GAPDH (#9272, #4060, #4695, #4370, and #5174, Cell Signaling, respectively) in 5% BSA in TBS-T with gentle rocking. The membrane was washed in TBS-T (3 × 5 min) before adding the HRP-conjugated secondary antibodies diluted 1:10,000 (anti-rabbit-HRP, GE Healthcare, #NA934V and anti-mouse-HRP, GE Healthcare, #NXA931) for 1 h at room temperature in 5% BSA in TBS-T with gentle rocking. The membrane was washed with TBS-T (3 × 5 min), and Western blots were visualized using Clarity Western ECL substrate (#1705061, Bio-Rad) with the Amersham ImageQuant 800 Western blot imaging system (Cytiva). the Western blots were quantified using ImageJ.

Confocal Laser Scanning Microscopy

For incorporation studies, the **V3** peptide was prepared through the reverse -phase evaporation technique as described previously at 10 μM in 0.1 mM of **BAIL** or 0.3 mM of **MAIL**. A control sample of the peptide with the same concentration was prepared in a homogeneous mixture of ACN:Milli-Q water. The dilution was performed using 25% glycerol in PB pH 7.4. The FAM-labeled molecules were excited in Ibidis tunnel slides at 488 nm and observed using laser scanning confocal ZEISS LSM 980 with Airyscan.

For localization studies, BT474 cells were seeded on a μ-slide 8 well high glass bottom at a density of 1.0×10^5 cells/well and incubated at 37 °C, 96% humidity, and 5% CO_2 for 24 h. The cells were further incubated for 2 h in RPMI-1640 medium containing 1.25 μM of **V3** peptide alone or in combination with the nanocarriers. The peptide was incorporated into the nanocarrier at their cac, 52 μM of **BAIL** and 150 μM of **MAIL**, using the reverse-phase evaporation technique. The cells were stained with CellMask deep red PM stain (Invitrogen) 5 μg/mL in PBS for 5 min at 37 °C and fixed with 4% formaldehyde in phosphate-buffered saline (PBS) for 10 min. Then, the cells were stained with DAPI for 5 min, washed three times with PBS between the staining steps, and following the fixation, the excess buffer was drained. ProLong Glass Antifade Mountant was added to the samples, and the cells were observed using laser scanning confocal ZEISS LSM 980 with Airyscan. DAPI, FAM, and the red membrane dye were

https://doi.org/10.1021/acsami.6c08450
ACS Appl. Mater. Interfaces XXXX, XXX, XXX–XXX

excited at 301 nm, 488 nm, and 637 nm, respectively, and observed in different channels by the use of suitable emission filter.

Statistical Analysis

Data are expressed as mean ± standard deviation (SD). Data were analyzed using one-way ANOVA. Statistical significance was set at $*p < 0.05$ and $**p < 0.01$.

■ ASSOCIATED CONTENT

Data Availability Statement

The details on the reaction progress, synthetic procedures, RP-HPLC chromatograms, physicochemical characterization of the nanocarriers, $^{1}H/^{13}C$ NMR spectra, cryo-EM and CLSM images are represented in Supporting Information.

Supporting Information

The Supporting Information is available free of charge at https://pubs.acs.org/doi/10.1021/acsami.6c08450.

Supplementary tables and figures, which provide NMR spectra and assignments, analytical characterization of peptides, including CD spectra and UV–vis peptide characterization, DSC and DLS of **MAIL** and **BAIL**, stability analysis, cryo-TEM imaging, planar lipid bilayer data, cell viability, bioinformatic analyses, cell viability and synergy studies, trastuzumab controls, western blot analyses, and live-cell imaging (DOCX)

■ AUTHOR INFORMATION

Corresponding Author

Alesia A. Tietze – *Department of Chemistry and Molecular Biology, Wallenberg Centre for Molecular and Translational Medicine, University of Gothenburg, Natrium, Medicinaregatan 7B, Gothenburg 41390, Sweden; Wallenberg Centre for Molecular and Translational Medicine, University of Gothenburg, Gothenburg 41390, Sweden;* orcid.org/0000-0002-9281-548X; Email: alesia.a.tietze@gu.se

Authors

Helal Abujubara – *Department of Chemistry and Molecular Biology, Wallenberg Centre for Molecular and Translational Medicine, University of Gothenburg, Natrium, Medicinaregatan 7B, Gothenburg 41390, Sweden; Wallenberg Centre for Molecular and Translational Medicine, University of Gothenburg, Gothenburg 41390, Sweden; Department of Pharmaceutical Science, Faculty of Pharmacy, Al-Ahliyya Amman University, Amman 19328, Jordan*

Pankaj Bharmoria – *Institute of Materials Science of Barcelona, ICMAB-CSIC, Bellaterra, Barcelona 08193, Spain; Department of Chemical Engineering, Universitat Politècnica de Catalunya, EEBE, Eduard Maristany 10–14, Barcelona 08019, Spain;* orcid.org/0000-0001-6573-0475

Dorota Raj – *Sahlgrenska Center for Cancer Research, Department of Surgery, Institute of Clinical Sciences, University of Gothenburg, Medicinaregatan 1F, Göteborg 41390, Sweden; Wallenberg Centre for Molecular and Translational Medicine, University of Gothenburg, Gothenburg 41390, Sweden*

Samantha W. Alvarez – *Sahlgrenska Center for Cancer Research, Department of Surgery, Institute of Clinical Sciences, University of Gothenburg, Medicinaregatan 1F, Göteborg 41390, Sweden; Wallenberg Centre for Molecular and Translational Medicine, University of Gothenburg, Gothenburg 41390, Sweden*

Siyuan Liu – *Department of Chemistry and Molecular Biology, Wallenberg Centre for Molecular and Translational Medicine, University of Gothenburg, Natrium, Medicinaregatan 7B, Gothenburg 41390, Sweden; Wallenberg Centre for Molecular and Translational Medicine, University of Gothenburg, Gothenburg 41390, Sweden*

Maryna Zhylinskaya – *Department of Chemistry and Molecular Biology, Wallenberg Centre for Molecular and Translational Medicine, University of Gothenburg, Natrium, Medicinaregatan 7B, Gothenburg 41390, Sweden; Wallenberg Centre for Molecular and Translational Medicine, University of Gothenburg, Gothenburg 41390, Sweden*

Enoch Appiah – *Department of Chemistry and Molecular Biology, Wallenberg Centre for Molecular and Translational Medicine, University of Gothenburg, Natrium, Medicinaregatan 7B, Gothenburg 41390, Sweden; Wallenberg Centre for Molecular and Translational Medicine, University of Gothenburg, Gothenburg 41390, Sweden*

Kasper Moth-Poulsen – *Institute of Materials Science of Barcelona, ICMAB-CSIC, Bellaterra, Barcelona 08193, Spain; Department of Chemical Engineering, Universitat Politècnica de Catalunya, EEBE, Eduard Maristany 10–14, Barcelona 08019, Spain; Catalan Institution for Research & Advanced Studies, ICREA, Pg. Lluís Companys 23, Barcelona 08010, Spain; Department of Chemistry and Chemical Engineering, Chalmers University of Technology, Gothenburg 41296, Sweden;* orcid.org/0000-0003-4018-4927

Clotilde Wiel – *Sahlgrenska Center for Cancer Research, Department of Surgery, Institute of Clinical Sciences, University of Gothenburg, Medicinaregatan 1F, Göteborg 41390, Sweden; Wallenberg Centre for Molecular and Translational Medicine, University of Gothenburg, Gothenburg 41390, Sweden*

Volkan I. Sayin – *Sahlgrenska Center for Cancer Research, Department of Surgery, Institute of Clinical Sciences, University of Gothenburg, Medicinaregatan 1F, Göteborg 41390, Sweden; Wallenberg Centre for Molecular and Translational Medicine, University of Gothenburg, Gothenburg 41390, Sweden*

Complete contact information is available at: https://pubs.acs.org/doi/10.1021/acsami.6c08450

Notes

The authors declare no competing financial interest.

■ ACKNOWLEDGMENTS

The Knut and Alice Wallenberg Foundation via the Wallenberg Centre for Molecular and Translational Medicine (A.A.T. and V.I.S.), Swedish Research Council (2025-05306 to A.A.T. and 2022-00971 to V.I.S.) and Cancerfonden (25-4861 to A.A.T. and 23-3062 to V.I.S.) are gratefully acknowledged. The authors acknowledge the Centre for Cellular Imaging at the University of Gothenburg and the National Microscopy Infrastructure, NMI (VR-RFI 2016-00968) for providing assistance in microscopy. P.B. acknowledges La-Caixa foundation under junior leadership programme for funding the project PHOLCEB (ID: 100010434, fellowship code: LCF/BQ/P122/11910023), and State Investigation Agency, through the Severo Ochoa Programme for Centres of Excellence in R&D

(CEX2023-001263-S), Ramón y Cajal grant (grant no. J03416) and Proyectos de Generación de Conocimiento (PID2024-160803NB-C32, grant no. J-03484) for financial support. K.M.-P. acknowledges European Research Council (ERC) under grant agreement CoG, PHOTHERM-101002131, the Catalan Institute of Advanced Studies (ICREA), and the European Union's Horizon 2020 Framework Programme under grant agreement no. 951801.

■ REFERENCES

(1) Behl, A.; Wani, Z. A.; Das, N. N.; Parmar, V. S.; Len, C.; Malhotra, S.; Chhillar, A. K. Monoclonal Antibodies in Breast Cancer: A Critical Appraisal. *Crit. Rev. Oncol. Hematol.* **2023**, *183*, 103915.

(2) Riudavets, M.; Sullivan, I.; Abdayem, P.; Planchard, D. Targeting HER2 in Non-Small-Cell Lung Cancer (NSCLC): a Glimpse of Hope? An Updated Review on Therapeutic Strategies in NSCLC Harbouring HER2 Alterations. *ESMO Open* **2021**, *6* (5), 100260.

(3) Furrer, D.; Paquet, C.; Jacob, S.; Diorio, C. The Human Epidermal Growth Factor Receptor 2 (HER2) as a Prognostic and Predictive Biomarker: Molecular Insights into HER2 Activation and Diagnostic Implications. *Cancer prognosis* **2018**, *5*, 11–21.

(4) Jahan, S.; Karim, M.; Chowdhury, E. Nanoparticles Targeting Receptors on Breast Cancer for Efficient Delivery of Chemotherapeutics. *Biomedicines* **2021**, *9* (2), 114.

(5) Agostinetto, E.; Curigliano, G.; Piccart, M. Emerging Treatments in HER2-Positive Advanced Breast Cancer: Keep Raising the Bar. *Cell Rep. Med.* **2024**, *5* (6), 101575.

(6) Omidi, Y.; Mobasher, M.; Castejon, A. M.; Mahmoudi, M. Recent Advances in Nanoscale Targeted Therapy of HER2-Positive Breast Cancer. *J. Drug Target.* **2022**, *30* (7), 687–708.

(7) Hamadani, C. M.; Dasanayake, G. S.; Gorniak, M. E.; Pride, M. C.; Monroe, W.; Chism, C. M.; Heintz, R.; Jarrett, E.; Singh, G.; Edgecomb, S. X. Development of Ionic Liquid-Coated PLGA Nanoparticles for Applications in Intravenous Drug Delivery. *Nat. Protoc.* **2023**, *18* (8), 2509–2557.

(8) Matczuk, M.; Timerbaev, A. R.; Keppler, B. K.; Ruzik, L. Ionic liquid-Mediated Drug Delivery: A Review on Progress and Challenges Focused on Poly (Ionic Liquid) Nanoplatforms. *J. Mol. Liq.* **2024**, *399*, 124403.

(9) Rebollo, R.; Niu, Z.; Blaabjerg, L.; La Zara, D.; Juel, T.; Pedersen, H. D.; Andersson, V.; Benova, M.; Krogh, C.; Pons, R. Salcaprozate-Based Ionic Liquids for GLP-1 Gastric Delivery: A Mechanistic Understanding of in Vivo Performance. *J. Control. Release* **2025**, *377*, 267–276.

(10) Shukla, M. K.; Tiwari, H.; Verma, R.; Dong, W. L.; Azizov, S.; Kumar, B.; Pandey, S.; Kumar, D. Role and Recent Advancements of Ionic Liquids in Drug Delivery Systems. *Pharmaceutics* **2023**, *15* (2), 702.

(11) Hu, Y.; Xing, Y.; Yue, H.; Chen, T.; Diao, Y.; Wei, W.; Zhang, S. Ionic Liquids Revolutionizing Biomedicine: Recent Advances and Emerging Opportunities. *Chem. Soc. Rev.* **2023**, *52* (20), 7262–7293.

(12) Musiał, M.; Olejniczak, A. B.; Denel-Bobrowska, M.; Zorebski, E.; Dzida, M. In Vitro Anticancer and Antivirus Activities of Cyano- and Bis (Trifluoromethylsulfonyl) Imide-Based Ionic Liquids. *ACS Sustainable Chem. Eng.* **2021**, *9* (48), 16459–16465.

(13) Leitch, A. C.; Abdelghany, T. M.; Charlton, A.; Grigalyte, J.; Oakley, F.; Borthwick, L. A.; Reed, L.; Knox, A.; Reilly, W. J.; Agius, L. Renal Injury and Hepatic Effects from the Methylimidazolium Ionic Liquid M8OI in Mouse. *Ecotoxicol. Environ. Saf.* **2020**, *202*, 110902.

(14) Tada, Y.; Yano, N.; Takahashi, H.; Yuzawa, K.; Ando, H.; Kubo, Y.; Nagasawa, A.; Ohashi, N.; Ogata, A.; Nakae, D. Toxicological Evaluation of l-Proline in a 90-day Feeding Study with Fischer 344 Rats. *Regul. Toxicol. Pharmacol.* **2010**, *58* (1), 114–120.

(15) Pandya, I.; Mishra, S.; Patel, T.; Keppeler, N.; Kumar, S.; Aswal, V. K.; Kailasa, S. K.; El Seoud, O.; Malek, N. I. 5-Fluoro Uracil Mediated Transformation of Surface-Active Ionic Liquid Based Micellar Nanoaggregates into pH-Responsive Vesicular Nanoaggregates as Promising Delivery Vehicle. *J. Mol. Liq.* **2024**, *409*, 125443.

(16) Moshikur, R. M.; Ali, M. K.; Moniruzzaman, M.; Goto, M. Recent Advances in Surface-Active Ionic Liquid-Assisted Self-Assembly Systems for Drug Delivery. *Curr. Opin. Colloid Interface Sci.* **2021**, *56*, 101515.

(17) Liu, T.; Zhang, D.; Pan, Z.; Yang, H.; Ruan, B.; Bo, Y.; Xie, L.; Wang, Z.; Zhang, J. Lysine-Based Ionic Liquid Enables Peptides to Reverse Skin Photoaging: From Leaves to Roots. *Adv. Funct. Mater.* **2023**, *33* (22), 2300723.

(18) Rühling, A.; Wang, D.; Ernst, J. B.; Wulff, S.; Honeker, R.; Richter, C.; Ferry, A.; Galla, H. J.; Glorius, F. Influence of the Headgroup of Azolium-Based Lipids on their Biophysical Properties and Cytotoxicity. *Chemistry* **2017**, *23* (25), 5920–5924.

(19) Rubin, E.; Shan, K. S.; Dalal, S.; Vu, D. U. D.; Milillo-Naraine, A. M.; Guaqueta, D.; Ergle, A. Molecular Targeting of the Human Epidermal Growth Factor Receptor-2 (HER2) Genes Across Various Cancers. *Int. J. Mol. Sci.* **2024**, *25* (2), 1064.

(20) Swain, S. M.; Shastry, M.; Hamilton, E. Targeting HER2-Positive Breast Cancer: Advances and Future Directions. *Nat. Rev. Drug Discovery* **2023**, *22* (2), 101–126.

(21) Rius Ruiz, I.; Vicario, R.; Morancho, B.; Morales, C. B.; Arenas, E. J.; Herter, S.; Freimoser-Grundschober, A.; Somandin, J.; Sam, J.; Ast, O.; Barriocanal, A. M.; Luque, A.; Escorihuela, M.; Varela, I.; Cuartas, I.; Nuciforo, P.; Fasani, R.; Peg, V.; Rubio, I.; Cortes, J.; Serra, V.; Escriva-de-Romani, S.; Sperinde, J.; Chenna, A.; Huang, W.; Winslow, J.; Albanell, J.; Seoane, J.; Scaltriti, M.; Baselga, J.; Tabernero, J.; Umana, P.; Bacac, M.; Saura, C.; Klein, C.; Arribas, J. P95HER2-T Cell Bispecific Antibody for Breast Cancer Treatment. *Sci. Transl. Med.* **2018**, *10* (461), eaat1445.

(22) Luca, S.; Verdoliva, V.; Saviano, M. Peptide Ligands Specifically Targeting HER2 Receptor and the Role Played by a Synthetic Model System of the Receptor Extracellular Domain: Hypothesized Future Perspectives. *J. Med. Chem.* **2020**, *63* (24), 15333–15343.

(23) Albrecht, C.; Appert-Collin, A.; Bagnard, D.; Blaise, S.; Romier-Crouzet, B.; Efremov, R. G.; Sartelet, H.; Duca, L.; Maurice, P.; Bennasroune, A. Transmembrane Peptides as Inhibitors of Protein-Protein Interactions: An Efficient Strategy to Target Cancer Cells?. *Front. Oncol.* **2020**, *10* (519), 519.

(24) Zhou, J.; Bian, X.; Kan, Z.; Cai, Z.; Jiang, Y.; Wang, Z.; Li, Y.; Shi, W.; Qian, H. In Silico Exploration and Biological Evaluation of Bispecific Peptides Derived from Anti-HER2 Antibodies and Peptide-Camptothecin Conjugates for HER2-Positive Breast Cancer. *J. Med. Chem.* **2022**, *65* (22), 15123–15139.

(25) Lofts, F. J.; Hurst, H. C.; Sternberg, M. J.; Gullick, W. J. Specific Short Transmembrane Sequences can Inhibit Transformation by the Mutant Neu Growth Factor Receptor in Vitro and in Vivo. *Oncogene* **1993**, *8* (10), 2813–2820.

(26) Bennasroune, A.; Fickova, M.; Gardin, A.; Dirrig-Grosch, S.; Aunis, D.; Cremel, G.; Hubert, P. Transmembrane Peptides as Inhibitors of ErbB Receptor Signaling. *Mol. Biol. Cell* **2004**, *15* (7), 3464–3474.

(27) Arpel, A.; Sawma, P.; Spenle, C.; Fritz, J.; Meyer, L.; Garnier, N.; Velazquez-Quesada, I.; Hussenet, T.; Aci-Seche, S.; Baumlin, N.; Genest, M.; Brasse, D.; Hubert, P.; Cremel, G.; Orend, G.; Laquerriere, P.; Bagnard, D. Transmembrane Domain Targeting Peptide Antagonizing ErB2/Neu Inhibits Breast Tumor Growth and Metastasis. *Cell Rep.* **2014**, *8* (6), 1714–1721.

(28) Bennasroune, A.; Gardin, A.; Auzan, C.; Clauser, E.; Dirrig-Grosch, S.; Meira, M.; Appert-Collin, A.; Aunis, D.; Cremel, G.; Hubert, P. Inhibition by Transmembrane Peptides of Chimeric Insulin Receptors. *Cell. Mol. Life Sci.* **2005**, *62* (18), 2124–2131.

(29) Zhou, Y. HER2/Neu-Based Vaccination with Li-key Hybrid, GM-CSF Immunoadjuvant and Trastuzumab as a Potent Triple-Negative Breast Cancer Treatment. *J. Cancer Res. Clin. Oncol.* **2023**, *149* (9), 6711–6718.

https://doi.org/10.1021/acsami.6c08450
ACS Appl. Mater. Interfaces XXXX, XXX, XXX–XXX

(30) Baumruck, A. C.; Tietze, D.; Steinacker, L. K.; Tietze, A. A. Chemical Synthesis of Membrane Proteins: A Model Study on the Influenza Virus B Proton Channel. *Chem. Sci.* **2018**, *9* (8), 2365–2375.
(31) Baumruck, A. C.; Tietze, D.; Stark, A.; Tietze, A. A. Reactions of Sulfur-Containing Organic Compounds and Peptides in 1-Ethyl-3-Methyl-Imidazolium Acetate. *J. Org. Chem.* **2017**, *82* (14), 7538–7545.
(32) Baumruck, A. C.; Yang, J.; Thomas, G. F.; Beyer, L. I.; Tietze, D.; Tietze, A. A. Native Chemical Ligation of Highly Hydrophobic Peptides in Ionic Liquid-Containing Media. *J. Org. Chem.* **2021**, *86* (2), 1659–1666.
(33) Abujubara, H.; Yang, J.; Birsen Otyakmaz, A.; Noisier, A. F. M.; Czechtizky, W.; Lemurell, M.; Tietze, A. A. Ionic Liquid-Mediated Approach for the Synthesis of Site-Specific Thioether Conjugates. *Chemistry* **2023**, *29* (28), e202203915.
(34) Weber, W.; Roeder, M.; Probanowski, T.; Yang, J.; Abujubara, H.; Koeppl, H.; Tietze, A.; Stein, V. Functional Nanopore Screen: A Versatile High-Throughput Assay to Study and Engineer Protein Nanopores in Escherichia Eoli. *ACS Synth. Biol.* **2022**, *11* (6), 2070–2079.
(35) Wu, S.; Li, F.; Zeng, L.; Wang, C.; Yang, Y.; Tan, Z. Assessment of the Toxicity and Biodegradation of Amino Acid-Based Ionic Liquids. *RSC Adv.* **2019**, *9* (18), 10100–10108.
(36) Poznik, M.; König, B. Enantioselective Ester Hydrolysis by an Achiral Catalyst Co-Embedded with Chiral Amphiphiles into a Vesicle Membrane. *RSC Adv.* **2016**, *6* (50), 44456–44458.
(37) Trivedi, T. J.; Rao, K. S.; Singh, T.; Mandal, S. K.; Sutradhar, N.; Panda, A. B.; Kumar, A. Task-Specific, Biodegradable Amino Acid Ionic Liquid Surfactants. *ChemSusChem* **2011**, *4* (5), 604–608.
(38) Rao, K. S.; Gehlot, P. S.; Gupta, H.; Drechsler, M.; Kumar, A. Sodium Bromide Induced Micelle to Vesicle Transitions of Newly Synthesized Anionic Surface Active Ionic Liquids Based on Dodecylbenzenesulfonate. *J. Phys. Chem. B* **2015**, *119* (11), 4263–4274.
(39) Kumar, A.; Dixit, C. K. Methods for Characterization of Nanoparticles. In *Advances in Nanomedicine for the Delivery of Therapeutic Nucleic Acids*; Nimesh, S.; Chandra, R.; Gupta, N., Eds.; Woodhead Publishing: Cambridge, **2017**; pp 43–58.
(40) Koshy, P.; Aswal, V. K.; Venkatesh, M.; Hassan, P. A. Swelling and Elongation of Tetradecyltrimethylammonium Bromide Micelles Induced by Anionic Sodium Laurate. *Soft Matter* **2011**, *7* (10), 4778–4786.
(41) Fang, J.; Nakamura, H.; Maeda, H. The EPR Effect: Unique Features of Tumor Blood Vessels for Drug Delivery, Factors Involved, and Limitations and Augmentation of the Effect. *Adv. Drug Delivery Rev.* **2011**, *63* (3), 136–151.
(42) Liu, X.; Liu, Y.; Han, Y.; Adnan, M.; Yu, S.; Qiu, B.; Yu, H.; Hou, S. The Size of Apoplastic Peptides: Do the Cell Wall Matrix and Cell-Surface Receptors Matter?. *Plant Commun.* **2026**, *7* (3), 101740.
(43) Lafarge, E. J.; Muller, P.; Schroder, A. P.; Zaitseva, E.; Behrends, J. C.; Marques, C. M. Activation Energy for Pore Opening in Lipid Membranes under an Electric Field. *Proc. Natl. Acad. Sci. U. S. A.* **2023**, *120* (11), e2213112120.
(44) Milton, R. C. D.; Milton, S. C. F.; Adams, P. A. Prediction of Difficult Sequences in Solid-Phase Peptide-Synthesis. *J. Am. Chem. Soc.* **1990**, *112* (16), 6039–6046.
(45) Paradis-Bas, M.; Tulla-Puche, J.; Albericio, F. The Road to the Synthesis of "Difficult Peptides". *Chem. Soc. Rev.* **2016**, *45* (3), 631–654.
(46) Mueller, L. K.; Baumruck, A. C.; Zhdanova, H.; Tietze, A. A. Challenges and Perspectives in Chemical Synthesis of Highly Hydrophobic Peptides. *Front. Bioeng. Biotechnol.* **2020**, *8*, 162.
(47) Paradís-Bas, M.; Albert-Soriano, M.; Tulla-Puche, J.; Albericio, F. Linear Versus Branched Poly-Lysine/Arginine as Polarity Enhancer Tags. *Org. Biomol. Chem.* **2014**, *12* (37), 7194–7196.
(48) Ma, J.; Yan, L.; Yang, J.; He, Y.; Wu, L. Effect of Modification Strategies on the Biological Activity of Peptides/Proteins. *ChemBioChem* **2024**, *25* (3), e202300481.
(49) Lavis, L. D. Teaching Old Dyes New Tricks: Biological Probes Built from Fluoresceins and Rhodamines. *Annu. Rev. Biochem.* **2017**, *86*, 825–843.
(50) Eiriksdottir, E.; Konate, K.; Langel, U.; Divita, G.; Deshayes, S. Secondary Structure of Cell-Penetrating Peptides Controls Membrane Interaction and Insertion. *Biochim. Biophys. Acta* **2010**, *1798* (6), 1119–1128.
(51) Rigaud, J. L.; Pitard, B.; Levy, D. Reconstitution of Membrane Proteins into Liposomes: Application to Energy-Transducing Membrane Proteins. *Biochim. Biophys. Acta* **1995**, *1231* (3), 223–246.
(52) Bharmoria, P.; Kumar, A. Thermodynamic Investigations of Protein's Behaviour with Ionic Liquids in Aqueous Medium Studied by Isothermal Titration Calorimetry. *Biochim. Biophys. Acta* **2016**, *1860* (5), 1017–1025.
(53) Gill, S. J.; Nichols, N. F.; Wadsö, I. Calorimetric Determination of Enthalpies of Solution of Slightly Soluble Liquids II Enthalpy of Solution of some Hydrocarbons in Water and their use in Establishing the Temperature Dependence of their Solubilities. *J. Chem. Thermodyn.* **1976**, *8* (5), 445–452.
(54) Pimentel, G. C.; Mcclella, A. Hydrogen Bonding. *Annu. Rev. Phys. Chem.* **1971**, *22*, 347.
(55) Broad DepMap. *Depmap 23Q4 Public*, **2023**. https://plus.figshare.com/articles/dataset/DepMap_23Q4_Public/24667905.
(56) Vraneš, M.; Tot, A.; Ćosić, J.; Papović, S.; Panić, J.; Gadžurić, S.; Janković, N.; Vrandečić, K. Correlation Between Lipophilicity of Newly Synthesized Ionic Liquids and Selected Fusarium Genus Growth Rate. *RSC Adv.* **2019**, *9* (33), 19189–19196.
(57) Kumari, P.; Pillai, V. V.; Benedetto, A. Mechanisms of Action of Ionic Liquids on Living Cells: The State of the Art. *Biophys. Rev.* **2020**, *12* (5), 1187–1215.
(58) Fu, M.; Zhuang, X.; Zhang, T.; Guan, Y.; Meng, Q.; Zhang, Y. Pegylated Leuprolide with Improved Pharmacokinetic Properties. *Bioorg. Med. Chem.* **2020**, *28* (4), 115306.
(59) Köhler, G.; Milstein, C. Continuous Cultures of Fused Cells Secreting Antibody of Predefined Specificity. *Nature* **1975**, *256* (5517), 495–497.
(60) Chou, T.C.; Talalay, P. Quantitative Analysis of Dose-Effect Relationships: The Combined Effects of Multiple Drugs or Enzyme Inhibitors. *Adv. Enzyme Regul.* **1984**, *22*, 27–55.
(61) Chou, T.-C.; Martin, N.*Compusyn for Drug Combinations and for General Dose-Effect Analysis*; ComboSyn, Inc.: Paramus, NJ, **2005**.
(62) Stawikowski, M.; Fields, G. B. Introduction to Peptide Synthesis. *Curr. Protoc. Protein Sci.* **2012**, *69* (1), 1–18.
(63) Abdul-Gader, A.; Miles, A. J.; Wallace, B. A. A Reference Dataset for the Analyses of Membrane Protein Secondary Structures and Transmembrane Residues using Circular Dichroism Spectroscopy. *Bioinformatics* **2011**, *27* (12), 1630–1636.
(64) Sreerama, N.; Woody, R. W. Estimation of Protein Secondary Structure from Circular Dichroism Spectra: Comparison of CONTIN, SELCON, and CDSSTR Methods with an Expanded Reference Set. *Anal. Biochem.* **2000**, *287* (2), 252–260.
(65) Whitmore, L.; Wallace, B. A. DICHROWEB, an Online Server for Protein Secondary Structure Analyses from Circular Dichroism Spectroscopic Data. *Nucleic Acids Res.* **2004**, *32*, W668–W673.
(66) Lobley, A.; Whitmore, L.; Wallace, B. A. DICHROWEB: an Interactive Website for the Analysis of Protein Secondary Structure from Circular Dichroism Spectra. *Bioinformatics* **2002**, *18* (1), 211–212.
(67) Braun, C. J.; Baer, T.; Moroni, A.; Thiel, G. Pseudo Painting/Air Bubble Technique for Planar Lipid Bilayers. *J. Neurosci. Methods* **2014**, *233*, 13–17.